



**NAVAL
POSTGRADUATE
SCHOOL**

MONTEREY, CALIFORNIA

THESIS

**ANALYSIS OF THE INFLUENCE OF TURBULENCE
AND ENVIRONMENTAL VARIABILITY ON
BROADBAND ACOUSTIC COHERENCE**

by

Ozer Eroglu

September 2004

Thesis Advisor:

Kevin B. Smith

Thesis Co-Advisor:

Samuel E. Buttrey

Approved for public release; distribution is unlimited.

THIS PAGE INTENTIONALLY LEFT BLANK

REPORT DOCUMENTATION PAGE		<i>Form Approved OMB No. 0704-0188</i>	
<p>Public reporting burden for this collection of information is estimated to average 1 hour per response, including the time for reviewing instruction, searching existing data sources, gathering and maintaining the data needed, and completing and reviewing the collection of information. Send comments regarding this burden estimate or any other aspect of this collection of information, including suggestions for reducing this burden, to Washington headquarters Services, Directorate for Information Operations and Reports, 1215 Jefferson Davis Highway, Suite 1204, Arlington, VA 22202-4302, and to the Office of Management and Budget, Paperwork Reduction Project (0704-0188) Washington DC 20503.</p>			
1. AGENCY USE ONLY (Leave blank)	2. REPORT DATE	3. REPORT TYPE AND DATES COVERED	
	September 2004	Master's Thesis	
4. TITLE AND SUBTITLE: Title (Mix case letters)		5. FUNDING NUMBERS	
Analysis Of The Influence Of Turbulence And Environmental Variability On Broadband Acoustic Coherence			
6. AUTHOR(S) LtJG Ozer Eroglu		8. PERFORMING ORGANIZATION REPORT NUMBER	
7. PERFORMING ORGANIZATION NAME(S) AND ADDRESS(ES) Naval Postgraduate School Monterey, CA 93943-5000		10. SPONSORING/MONITORING AGENCY REPORT NUMBER	
9. SPONSORING /MONITORING AGENCY NAME(S) AND ADDRESS(ES) N/A			
11. SUPPLEMENTARY NOTES The views expressed in this thesis are those of the author and do not reflect the official policy or position of the Department of Defense or the U.S. Government.			
12a. DISTRIBUTION / AVAILABILITY STATEMENT Approved for public release; distribution is unlimited.		12b. DISTRIBUTION CODE	
13. ABSTRACT (maximum 200 words) Acoustic propagation in the littoral regions of the world, even over short ranges, can be complex at high frequencies (> 5 kHz), and applications such as underwater detection and communications suffer as a result. To this end, the Asian Seas International Acoustics Experiment (ASIAEX) was conducted with funding from the Office of Naval Research. One phase of this experiment took place from 29 May to 9 June 2001 and focused on short-range, shallow water acoustic propagation in the East China Sea. This thesis will be based on some of the measurements taken during the East China Sea experiment by a team from the Applied Physics Laboratory of the University of Washington. The environmental parameters and array geometry used in this and previous modeling work are as close as possible to the experiment.			
The objective of this thesis is to better understand the nature of turbulent perturbations and how they affect short-range acoustic propagation in a shallow water environment. This will include variations in total energy of the turbulence, variations in associated length scales, and variations in depth. In addition, the influence of other variable factors on signal coherence will also be examined. Most notably, variations in background sound-speed structure and source depth variability will be included.			
14. SUBJECT TERMS Shallow water variability, turbulence, vertical coherence, sound speed curvature		15. NUMBER OF PAGES 95	
		16. PRICE CODE	
17. SECURITY CLASSIFICATION OF REPORT Unclassified	18. SECURITY CLASSIFICATION OF THIS PAGE Unclassified	19. SECURITY CLASSIFICATION OF ABSTRACT Unclassified	20. LIMITATION OF ABSTRACT UL

NSN 7540-01-280-5500

Standard Form 298 (Rev. 2-89)
Prescribed by ANSI Std. Z39-18

THIS PAGE INTENTIONALLY LEFT BLANK

Approved for public release; distribution is unlimited.

**ANALYSIS OF THE INFLUENCE OF TURBULENCE AND ENVIRONMENTAL
VARIABILITY ON BROADBAND ACOUSTIC COHERENCE**

Ozer Eroglu
Lieutenant Junior Grade, Turkish Navy
B.S., Turkish Naval Academy, 1998

Submitted in partial fulfillment of the
requirements for the degrees of

**MASTER OF SCIENCE IN ENGINEERING ACOUSTICS
&
MASTER OF SCIENCE IN OPERATIONS RESEARCH**

from the

**NAVAL POSTGRADUATE SCHOOL
September 2004**

Author: Ozer Eroglu

Approved by: Kevin B. Smith
Thesis Advisor

Samuel E. Buttrey
Co-Advisor

Kevin B. Smith, Chairman
Engineering Acoustics Academic Committee

James N. Eagle, Chairman
Department of Operations Research

THIS PAGE INTENTIONALLY LEFT BLANK

ABSTRACT

Acoustic propagation in the littoral regions of the world, even over short ranges, can be complex at high frequencies (> 5 kHz), and applications such as underwater detection and communications suffer as a result. To this end, the Asian Seas International Acoustics Experiment (ASIAEX) was conducted with funding from the Office of Naval Research. One phase of this experiment took place from 29 May to 9 June 2001 and focused on short-range, shallow water acoustic propagation in the East China Sea. This thesis will be based on some of the measurements taken during the East China Sea experiment by a team from the Applied Physics Laboratory of the University of Washington. The environmental parameters and array geometry used in this and previous modeling work are as close as possible to the experiment.

The objective of this thesis is to better understand the nature of turbulent perturbations and how they affect short-range acoustic propagation in a shallow water environment. This will include variations in total energy of the turbulence, variations in associated length scales, and variations in depth. In addition, the influence of other variable factors on signal coherence will also be examined. Most notably, variations in background sound-speed structure and source depth variability will be included.

THIS PAGE INTENTIONALLY LEFT BLANK

TABLE OF CONTENTS

I. INTRODUCTION.....	1
II. NUMERICAL METHODS AND IMPLEMENTATION	5
A. MONTEREY-MIAMI PARABOLIC EQUATION (MMPE) MODEL.....	5
B. TURBULENT SOUND-SPEED PERTURBATION THEORY.....	9
C. IMPLEMENTATION METHODS	14
1. Numerical Implementation of Turbulence	14
2. Creation of Source Spectrum.....	18
3. Direct Path Extraction.....	25
4. Vertical Spatial Correlation.....	27
III. MODEL VARIABLES	29
A. EXPERIMENTAL AND MODEL GEOMETRY	29
1. Source Depth	30
B. ENVIRONMENTAL MODELS	31
1. Turbulence Strength.....	32
2. Turbulence Outer Length Scale	32
3. Sound Speed Profiles	36
IV. POST PROCESSING AND ANALYSIS	39
A. TURBULENCE STRENGTH	39
B. TURBULENCE OUTER LENGTH SCALE.....	45
C. CURVATURE ANALYSIS.....	51
D. SOURCE DEPTH.....	56
E. SOUND-SPEED PROFILE.....	63
V. SUMMARY	71
A. CONCLUSIONS	71
B. RECOMMENDATIONS AND FUTURE WORK.....	72
LIST OF REFERENCES	75
INITIAL DISTRIBUTION LIST	77

THIS PAGE INTENTIONALLY LEFT BLANK

LIST OF FIGURES

Figure 1. Sample realization of the turbulent sound speed perturbations in m/s. The RMS sound speed fluctuation is 0.41 m/s.	17
Figure 2. Pulse arrival structure for a source depth of 50m, RMS sound speed perturbation of about 1 m/s, and an outer cutoff length of 10m.	19
Figure 3. Square filter function representing a 2 msec pulse.	21
Figure 4. Source spectrum created from 2 msec square window with a bandwidth of 8184 Hz.	23
Figure 5. Typical Hanning Signal-Processing Window	24
Figure 6. Extended source spectrum overlaid with 8 kHz bandpass filter. In this case, a carrier frequency of 20 kHz is used, thus requiring a 1 kHz shift.	25
Figure 7. Pressure time series received at shallow and deep depths at a range of 500 meters. Lo is the outer cutoff length, and RMS is the RMS value of the sound speed perturbation.	26
Figure 8. Extraction of the Direct Path Arrival.	27
Figure 9. Experimental Geometry from ASIAEX	29
Figure 10. Model Geometry Used in This Research	31
Figure 12. One-dimensional energy density spectra for reference outer length scale (10 m) and values below (2m and 5m). Vertical lines are the Fresnel radius values for 4, 8, 16, and 20 kHz, from left to right, respectively.	34
Figure 13. One-dimensional energy density spectra for reference outer length scale (10 m) and values above (25m and 50m). Vertical lines are the Fresnel radius values for 4, 8, 16, and 20 kHz, from left to right, respectively.	35
Figure 14. One-dimensional energy density spectra for reference outer length scale (10 m) and values above (25m and 50m) on a smaller scale. Vertical lines are the Fresnel radius values for 4, 8, 16, and 20 kHz, from left to right, respectively.	35
Figure 11. Sound Speed Profiles Used in the Modeling Analysis.	37
Figure 15. Effect of Turbulence Strength Parameter at 4 kHz.	41
(a) Turbulence Strength = Reference, (b) Turbulence Strength = Ref-2, (c) Turbulence Strength = Ref-1, (d) Turbulence Strength = Ref+1, (e) Turbulence Strength = Ref+2.	41
Figure 16. Effect of Turbulence Strength Parameter at 8 kHz.	42
(a) Turbulence Strength = Reference, (b) Turbulence Strength = Ref-2, (c) Turbulence Strength = Ref-1, (d) Turbulence Strength = Ref+1, (e) Turbulence Strength = Ref+2.	42
Figure 17. Effect of Turbulence Strength Parameter at 16 kHz.	43
(a) Turbulence Strength = Reference, (b) Turbulence Strength = Ref-2, (c) Turbulence Strength = Ref-1, (d) Turbulence Strength = Ref+1, (e) Turbulence Strength = Ref+2.	43
Figure 18. Effect of Turbulence Strength Parameter at 20 kHz.	44

(a) Turbulence Strength = Reference, (b) Turbulence Strength = Ref-2, (c) Turbulence Strength = Ref-1, (d) Turbulence Strength = Ref+1, (e) Turbulence Strength = Ref+2.....	44
Figure 19. Effect of Turbulence Outer Length Scale at 4 kHz.....	47
(a) Turbulence Scale = 10 m (Reference Case), (b) Turbulence Scale = 2 m, (c) Turbulence Scale = 5 m, (d) Turbulence Scale = 25 m, (e) Turbulence Scale = 50 m	47
Figure 20. Effect of Turbulence Outer Length Scale at 8 kHz.....	48
(a) Turbulence Scale = 10 m (Reference Case), (b) Turbulence Scale = 2 m, (c) Turbulence Scale = 5 m, (d) Turbulence Scale = 25 m, (e) Turbulence Scale = 50 m	48
Figure 21. Effect of Turbulence Outer Length Scale at 16 kHz.....	49
(a) Turbulence Scale = 10 m (Reference Case), (b) Turbulence Scale = 2 m, (c) Turbulence Scale = 5 m, (d) Turbulence Scale = 25 m, (e) Turbulence Scale = 50 m	49
Figure 22. Effect of Turbulence Outer Length Scale at 20 kHz.....	50
(a) Turbulence Scale = 10 m (Reference Case), (b) Turbulence Scale = 2 m, (c) Turbulence Scale = 5 m, (d) Turbulence Scale = 25 m, (e) Turbulence Scale = 50 m	50
Figure 23. Measured Sound speed Data Compared to Cubic Spline Fit for CTM Profile.....	52
Figure 24. Profiles of $\log U $ for the four environmental profiles examined: reference (upper left); CTM (upper right); MDD (lower left); MDU (lower right).....	53
Figure 25. Sample ray paths for the reference environment and the corresponding profiles of the along-ray mean of $\log U $ for three source depths: 30m (upper plots); 50m (middle plots); 70m (lower plots).....	55
Figure 26. Effect of Source Depth Variation at 4 kHz.....	59
(a) Source Depth = 50 m (Reference Case), (b) Source Depth = 30 m, (c) Source Depth = 40 m, (d) Source Depth = 60 m, (e) Source Depth = 70 m.....	59
Figure 27. Effect of Source Depth Variation at 8 kHz.....	60
(a) Source Depth = 50 m (Reference Case), (b) Source Depth = 30 m, (c) Source Depth = 40 m, (d) Source Depth = 60 m, (e) Source Depth = 70 m.....	60
Figure 28. Effect of Source Depth Variation at 16 kHz.....	61
(a) Source Depth = 50 m (Reference Case), (b) Source Depth = 30 m, (c) Source Depth = 40 m, (d) Source Depth = 60 m, (e) Source Depth = 70 m.....	61
Figure 29. Effect of Source Depth Variation at 20 kHz.....	62
(a) Source Depth = 50 m (Reference Case), (b) Source Depth = 30 m, (c) Source Depth = 40 m, (d) Source Depth = 60 m, (e) Source Depth = 70 m.....	62
Figure 30. Effect of Background Sound-Speed Profile at 4 kHz.....	66
(a) SSP = Reference Case, (b) SSP = CTM, (c) SSP = MDD, (d) SSP = MDU	66
Figure 31. Effect of Background Sound-Speed Profile at 8 kHz.....	67
(a) SSP = Reference Case, (b) SSP = CTM, (c) SSP = MDD, (d) SSP = MDU	67
Figure 32. Effect of Background Sound-Speed Profile at 16 kHz.....	68
(a) SSP = Reference Case, (b) SSP = CTM, (c) SSP = MDD, (d) SSP = MDU	68
Figure 33. Effect of Background Sound-Speed Profile at 20 kHz.....	69

(a) SSP = Reference Case, (b) SSP = CTM, (c) SSP = MDD, (d) SSP = MDU69

THIS PAGE INTENTIONALLY LEFT BLANK

LIST OF TABLES

Table 1. Characteristics of the bandpass filters used in data processing for each experimental carrier frequency. The required shift is the difference between the center of the filter and the experimental carrier frequency.	22
Table 2. RMS Perturbation of Sound Speed (m/s) for Different Turbulent Strengths	32
Table 3. Fresnel Radius and Fresnel Wavenumber Values for Different Frequencies at a Range of 500 m.....	33
Table 4. RMS Perturbation of Sound Speed (m/s) for Different Cases of Turbulence Outer Length Scale Parameter	36
Table 5. Sub-Array Averages of Along-Ray Means of $\log U $	57
Table 6. Sub-Array Averages of Correlation Values for Source Depth = 50 meters.	58
Table 7. Sub-Array Averages of Correlation Values for Source Depth = 60 meters.	58
Table 8. Sub-Array Averages of Correlation Values for Source Depth = 70 meters.	58
Table 9. Sub-array averages of along-ray means of $\log U $ for the source at 50 m depth.....	64
Table 10. Sub-Array Averages of Correlation Values for the reference SSP.....	64
Table 11. Sub-Array Averages of Correlation Values for the CTM sound speed profile.	65

THIS PAGE INTENTIONALLY LEFT BLANK

ACKNOWLEDGMENTS

The decision of completing two programs in NPS was hard to make. There had been many times I felt regretful about my decision and almost gave up throughout this education period. But, even when I fell and was almost creeping morally, I have always felt two people from thousands of miles away; tapping my back and making me stand up again. These are my most beloveds, my mother Halime and my father Emrah. Whatever I have accomplished so far, it should belong to them as much as me.

A special appreciation is for Professor Kevin Smith. I could have only finished this work by help of a very self-sacrificing and philanthropist person like him. There was no way to complete this thesis without his very endless help and knowledge.

Another special appreciation goes to Professor Sam Buttrey. Though the subject of this thesis was not in his field of specialization, he agreed and worked with us. I must thank him for his very important time and support.

There are so many to thank and list here but some of them include: CDR John Joseph (USW Curricular Officer), Professor James Sanders (former USW Academic Associate), Professor Daphne Kapolka (USW Academic Associate), Professor James Eagle (OA Chairman), Professor Robert Dell (OA Academic Associate), Eva Anderson (Code 35 Educational Specialist), and Donna Carpenter (International Programs Admin. Assistant).

THIS PAGE INTENTIONALLY LEFT BLANK

I. INTRODUCTION

Having the ability to perform operations in the littoral regions of the world is one of the most crucial issues if a navy intends to be fully capable. Since these regions differ from the so-called “blue waters” in many ways, even the most thorough deep water research may not be applicable. One of the most extensive researches conducted in littoral regions was the Asian Seas International Acoustics Experiment (ASIAEX), funded by the Office of Naval Research. The second phase of this project took place in the East China Sea (ECS).

One component of the ECS experiment involved the analysis of acoustic signal coherence over the length of a vertical array at relatively short range (500 m) from a controlled source. For certain source/receiver geometries, direct path arrivals, single surface bounce, and single bottom bounce paths could be distinguished, allowing analysis of coherence for those paths independently.

Previous thesis work done by LT Stephen C. Karpi at the Naval Postgraduate School contributed to the analysis of the direct path (no boundary reflections) arrivals by numerically evaluating the influence of various shallow water sound speed perturbations. Karpi’s research employed vertical coherence to measure the effects of longer scale, internal wave-like structures and smaller scale, turbulent-like fluctuations on the direct path propagation. His work showed that perturbations by an internal wave-like structure affected the coherence only slightly. However, turbulent-like fluctuations caused significant signal decorrelation RMS.

This thesis examines both the model geometry, including source and receiver depths, and the environmental variables, which are background sound-speed profile, turbulence strength and the turbulence outer length scale. The general geometry and source characteristics used during the East China Sea experiment by Peter Dahl of the Applied Physics Laboratory of the University of Washington are the basis of numerical studies in this thesis.

The model used in this work is the Monterey-Miami Parabolic Equation (MMPE) propagation model. The MMPE model was developed by Smith and Tappert in 1996. The specific version used in this work incorporates the range-dependent turbulent fluctuations and the source spectrum characteristics employed in the ASIAEX experiment. This model provides an efficient algorithm for computing the broadband source response in such range-dependent environments.

A realistic turbulence spectrum has multiple parameters which depend on various features of the ocean environment. In this work, only two parameters, a strength parameter to adjust the overall RMS value, and an outer length scale beyond which fluctuations have no contribution, will be considered variables. As a reference, 10 m is used for the outer length scale, and four other different values are tested. Because only weak scattering is expected, the outer length scale is not expected to directly affect the propagation. However, the dominant contribution to the scattering is expected to be at the Fresnel radius, and this is on the same order as the reference scale of 10 m. Thus, we may expect to see some differences with changes in the outer scale due to the energy in the turbulent perturbation near the Fresnel scale. Conversely, the turbulence strength parameter is expected to have a direct effect on scattering, and thus affect the signal coherence.

Besides the two aforementioned parameters of turbulence, the effects of variable background sound-speed profiles are examined in this research. The reference sound-speed profile (SSP) is taken as the average value of the measurements from ASIAEX. Three more SSPs are also examined. One of them is very close to the reference case, but has more variability along the depth. The other two are very different from the reference case. One of them has a much deeper thermocline and steeper gradient below, while the other has a shallower thermocline and generally less steep gradient below. The effects of SSP are examined using not only the vertical correlation but also using some simple ray tracing analysis involving sound-speed relative curvature (Duda et al, 1994).

The last variables investigated in this work are source and receiver depths. Since the model computes the propagation at all depths, no additional computational effort is

required to obtain the solution at any receiver depth. To compute vertical coherence, short sub-arrays are modeled by extracting the solution over 5 m vertical spans. The receiver sub-array depths that are analyzed are 35-40, 45-50, 55-60, and 65-70 m. The reference value used for source depth is 50 m, while 30, 40, 60, and 70 m are also tested. It should be noted that above 30 m or below 70 m of the source or receiver depths, the direct path propagation will overlap with those arrivals from surface scattering and bottom reflections, for the 2 msec pulse modeled. Since the focus of this work is to deal with the direct path propagation, these depths are disregarded in the analysis range.

Chapter II contains an overview of the theory behind the MMPE model and the turbulent spectrum. The implementation of these models and the post-processing methods are also examined in this chapter. Different model parameters and their range of analysis are covered in Chapter III. Chapter IV focuses on post-processing and the analysis of modeled data. The last chapter presents conclusions derived from the analysis and suggestions for future research.

THIS PAGE INTENTIONALLY LEFT BLANK

II. NUMERICAL METHODS AND IMPLEMENTATION

A. MONTEREY-MIAMI PARABOLIC EQUATION (MMPE) MODEL

The parabolic equation (PE) method was introduced into underwater acoustics in the early 1970's by Tappert. Due to its efficient numerical algorithm for computing solutions to general range-dependent problems, it has become the most popular method for computing the acoustic field in complex underwater acoustic environments. The MMPE model, developed by Smith and Tappert in the early 1990's, is based upon the parabolic equation method. In this chapter, a simple derivation of the MMPE model is described by borrowing heavily from Smith's descriptions.

We begin by defining the time-harmonic acoustic field in a cylindrical coordinate system by

$$P(r, z, \varphi, \omega t) = p(r, z, \varphi) e^{-i\omega t} . \quad (1)$$

Substituting Eq. (1) into the linearized acoustic wave equation in cylindrical coordinates leads to the Helmholtz equation,

$$\frac{1}{r} \frac{\partial}{\partial r} \left(r \frac{\partial p}{\partial r} \right) + \frac{1}{r^2} \frac{\partial^2 p}{\partial \varphi^2} + \frac{\partial^2 p}{\partial z^2} + k_0^2 n^2(r, z, \varphi) p = -4\pi P_0 \delta(\vec{x} - \vec{x}_s) , \quad (2)$$

where

$$k_0 = \omega / c_0 , \quad (3)$$

is the reference wavenumber, and

$$n(r, z, \varphi) = \frac{c_0}{c(r, z, \varphi)} \quad (4)$$

is the acoustic index of refraction. In Eq. (4), c_0 is the reference sound-speed and $c(r, z, \varphi)$ is the acoustic sound-speed. Note that $c(r, z, \varphi)$ carries all the information about the environment, except the density, which is unimportant in this development since we are only interested in propagation in the water column. Eq. (2) implies that the

source function is a point source at coordinates ($r = 0, z = z_s$) and has a source level of P_0 , which is defined as the pressure amplitude at a reference distance of $R_0 = 1\text{ m}$.

We may simplify this expression by defining the pressure field as

$$p(r, z) = \frac{1}{\sqrt{r}} u(r, z) . \quad (5)$$

Substitution into Eq. (2) yields the homogenous equation,

$$\frac{\partial^2 u}{\partial r^2} + \frac{1}{r^2} \frac{\partial u^2}{\partial \varphi^2} + \frac{\partial^2 u}{\partial z^2} + k_o^2 \left(n^2 + \frac{1}{4k_o^2 r^2} \right) u = 0 . \quad (6)$$

The last term in Eq. (6) decreases quickly due to $1/r^2$ dependence and is generally neglected. The second term accounts for azimuthal coupling between different radials and is small enough to consider as negligible. Neglecting this term is referred to as the “uncoupled azimuth (UNCA) approximation.”

The remaining Helmholtz equation can be further simplified by introducing the operator notations

$$P_{op} = \frac{\partial}{\partial r}, \quad \text{and} \quad Q_{op} = (\mu + \varepsilon + 1)^{\frac{1}{2}}, \quad (7)$$

where

$$\varepsilon = n^2 - 1, \quad \mu = \frac{1}{k_o^2} \frac{\partial^2}{\partial z^2} . \quad (8)$$

Eq. (6) can then be represented in the form

$$(P_{op}^2 + k_o^2 Q_{op}^2) u = 0 . \quad (9)$$

Factoring Eq. (9), outward and inward fields are represented in the form,

$$(P_{op} + ik_0 Q_{op})(P_{op} - ik_0 Q_{op}) u + ik_0 [P_{op}, Q_{op}] u = 0 \quad (10)$$

Assuming weak range dependence, the commutator $[P_{op}, Q_{op}]$ is negligible.

Furthermore, defining the outward propagating field as

$$u = \frac{1}{\sqrt{Q_{op}}} \Psi, \quad (11)$$

the outgoing solution satisfies

$$P_{op}\Psi = ik_0 Q_{op}\Psi \quad \text{or} \quad -ik_o^{-1} \frac{\partial \Psi}{\partial r} = Q_{op}\Psi . \quad (12)$$

If the backscattered energy is negligible, Eq. (12) represents the complete description of the forward propagating acoustic energy in the waveguide. This equation is the foundation for all underwater acoustic PE models.

To solve the parabolic equation given in Eq. (12), first the field should be decomposed into two parts, an envelope function and a phase term. A reasonable decomposition for the PE field function is defined by

$$\Psi = \psi(r, z) e^{ik_0 r} . \quad (13)$$

Using this modulating function, we get the PE for the field function in the form

$$\frac{\partial \psi}{\partial r} = ik_o (Q_{op} - 1) \psi . \quad (14)$$

PE solutions are based on developing an approximation to the pseudo-differential operator Q_{op} . There are basically three methods to solve the PE: the Finite Element (FE) method; the Finite Difference (FD) method; and the Split-Step Fourier (SSF) method. An approximation well suited for the SSF algorithm, on which the MMPE model is based, was introduced by Thompson and Chapman (1983) and is commonly referred to as the wide-angle PE (T-C WAPE). This approximation generally provides good accuracy in phase.

To obtain the SSF algorithm, let us rewrite the PE in terms of the Hamiltonian-like operator as

$$\frac{\partial \psi}{\partial r} = -ik_o H_{op} \psi , \quad (15)$$

where

$$H_{op} = 1 - Q_{op} . \quad (16)$$

This Hamiltonian-like operator defines the evolution of the PE field function in range. Solutions of the Ψ function at different ranges can be defined by a marching algorithm of the form

$$\psi(r + \Delta r) = \Phi(r)\psi(r) , \quad (17)$$

where $\Phi(r)$ is a unitary operator that progresses the solution out in range. The propagator $\Phi(r)$ can be approximated as

$$\Phi(r) \approx e^{-ik_0 \overline{H}_{op}(r)\Delta r} , \quad (18)$$

where

$$\overline{H}_{op}(r) = \frac{1}{\Delta r} \int_r^{r+\Delta r} dr' H_{op}(r') . \quad (19)$$

The advantage of the SSF algorithm is based on the fact that H_{op} is separated into a combination of spatial and differential operators, which can be expressed as

$$H_{op} = T_{op} + U_{op} , \quad (20)$$

where

$$U_{op} = -\left[\sqrt{1+\varepsilon} - 1 \right] = -(1-n) , \quad (21)$$

and

$$T_{op} = 1 - \sqrt{1+\mu} = 1 - \left[1 + \frac{1}{k_0^2} \frac{\partial^2}{\partial z^2} \right] . \quad (22)$$

Keeping in mind the assumptions made thus far, the propagator can be made 2nd order accurate in range step (Δr) by employing the form,

$$\Phi(r) = \left[e^{-ik_0 \frac{\Delta r}{2} U_{op}(r+\Delta r)} \right] \left[e^{-ik_0 \Delta r T_{op}} \right] \left[e^{-ik_0 \frac{\Delta r}{2} U_{op}(r)} \right] . \quad (23)$$

The operator U_{op} is a multiplication operator in the z -space and, hence, is a diagonal matrix. The operator T_{op} is not diagonal in the z -space, but it is in wavenumber space; therefore, the k_z -domain operator \tilde{T}_{op} is desired.

It is now possible to outline how the PE/SSF algorithm steps out in range. To begin, the PE field function is defined at some range, r , in the z -domain. This function is then multiplied by the operator, $e^{-ik_o * \Delta r / 2 * U_{op}(r)}$, defined at the beginning of the range step. A transformation to the k_z -domain then occurs so that we can multiply by $e^{-ik_o \Delta r \hat{T}_{op}}$. This result is then transferred back to the z -domain to be multiplied by the z -space operator defined at the end of the range step, $e^{-ik_o * \Delta r / 2 * U_{op}(r + \Delta r)}$. The discrete fast Fourier Transform (FFT) is being used in the code assuming the convention

$$\psi(z) = FFT(\hat{\psi}(k_z)) \quad (24)$$

and

$$\hat{\psi}(k_z) = IFFT(\psi(z)) . \quad (25)$$

The PE/SSF implementation can then be represented by

$$\psi(r + \Delta r, z) = e^{-ik_o \frac{\Delta r}{2} U_{op}(r + \Delta r, z)} FFT \left[e^{-ik_o \Delta r \hat{T}_{op}(k_z)} * IFFT \left(e^{-ik_o \frac{\Delta r}{2} U_{op}(r, z)} \psi(r, z) \right) \right], \quad (26)$$

where

$$\hat{T}_{op}(k_z) = 1 - \left[1 - \left(\frac{k_z}{k_0} \right)^2 \right]^{1/2} . \quad (27)$$

B. TURBULENT SOUND-SPEED PERTURBATION THEORY

Acoustic propagation through a medium is subject to the properties of that medium. When a spherical wavefront from a point source traverses a medium containing fluctuations in sound speed, portions of the front travel faster or slower than other parts of the wavefront and the front distorts as a result. In the ocean, such sound-speed inhomogeneities result from phenomena like layering, internal waves, and turbulence (Duda, et al, 1988). In this work, it is assumed that perturbations of sound speed are generated purely by turbulent fluctuations. These fluctuations are characterized using statistical relationships developed in previous work (Tatarskii, 1961; Duda, et al, 1988).

The statistical theory of turbulence characterizes the turbulent perturbation field as realizations of a random function. Such a characterization is only valid when changes in signal amplitude, due to fluctuations in the medium, do not exceed the average amplitude of the signal. This is referred to as the “weak scattering regime” (Duda et al, 1988).

If we define the index of refraction perturbation as

$$\delta n(\vec{r}) = \frac{\delta c(\vec{r})}{c(\vec{r})} \equiv \mu(\vec{r}), \quad (28)$$

then the variance of $\mu(\vec{r})$ is related to the spectral density of the perturbations, $S_\mu(\vec{K})$, by

$$\text{var}(\mu(\vec{r})) = \frac{1}{(2\pi)^3} \int_{-\infty}^{\infty} S_\mu(\vec{K}) d^3 K, \quad (29)$$

where the integral is a three-dimensional integral over all wavenumber space. The variance is defined by

$$\text{var}(\mu(\vec{r})) = \left\langle |\mu(\vec{r})|^2 \right\rangle = \frac{1}{\text{volume}} \int_V \mu^2(\vec{r}) d^3 r, \quad (30)$$

so

$$\int_V \mu^2(\vec{r}) d^3 r = \frac{\text{volume}}{(2\pi)^3} \int_{-\infty}^{\infty} S_\mu(\vec{K}) d^3 K. \quad (31)$$

If we define the spectrum (transform) of $\mu(\vec{r})$ as $F_\mu(\vec{K})$ by

$$\mu(\vec{r}) = \frac{1}{(2\pi)^3} \int_{-\infty}^{\infty} F_\mu(\vec{K}) e^{i\vec{K} \cdot \vec{r}} d^3 K, \quad (32)$$

then the correlation of $\mu(\vec{r})$ satisfies

$$\int_{-\infty}^{\infty} \mu(\vec{r}) \mu^*(\vec{r} - \vec{r}') d^3 r = \frac{1}{(2\pi)^3} \int_{-\infty}^{\infty} d^3 K |F_\mu(\vec{K})|^2 e^{i\vec{K}' \cdot \vec{r}'}. \quad (33)$$

Thus, $|F_\mu(\vec{K})|^2$ is the Fourier transform of the correlation function. It is easy to see that by setting $\vec{r}' = 0$, the square of the signal spectrum and the spectral density are related by

$$|F_\mu(\vec{K})|^2 = (\text{volume}) * S_\mu(\vec{K}). \quad (34)$$

It follows then that

$$|F_\mu(\vec{K})| = \left[\text{volume} * S_\mu(\vec{K}) \right]^{1/2}. \quad (35)$$

Note that $\mu(\vec{r})$ is unitless while $F_\mu(\vec{K})$ and $S_\mu(\vec{K})$ both have units of m^3 .

Similar reasoning holds for a two-dimensional slice at a fixed value of one variable, e.g. $\mu(x, y = 0, z)$, such that

$$\frac{1}{\text{Area}} \iint_A \mu^2(x, y = 0, z) dx dz = \frac{1}{(2\pi)^2} \int_{-\infty}^{\infty} \int_{-\infty}^{\infty} V_\mu(K_x, K_z) dK_x dK_z, \quad (36)$$

where $V_\mu(K_x, K_z) \equiv V_\mu(k_x, k_z, k_y = 0)$ is the two-dimensional spectral density along the slice $y = 0$. Furthermore,

$$\mu(x, z) = \frac{1}{(2\pi)^2} \int_{-\infty}^{\infty} \int_{-\infty}^{\infty} G_\mu(k_x, k_z) e^{i(k_x x + k_z z)} dk_x dk_z, \quad (37)$$

where $G_\mu(k_x, k_z)$ is the spectrum (transform) of the two-dimensional perturbation field. It follows that

$$|G_\mu(k_x, k_z)| = \left[\text{Area} * V_\mu(k_x, k_z) \right]^{1/2}. \quad (38)$$

The two-dimensional spectral density can be obtained from the three-dimensional spectral density according to (Tatarskii, 1961),

$$V_\mu(k_x, k_z) = \frac{1}{2\pi} \int_{-\infty}^{\infty} S_\mu(k_x, k_y, k_z) dk_y. \quad (39)$$

At this point in the turbulent analysis, perturbations in sound speed have been related to the spectral density of the turbulent fluctuations. Developing an expression for the turbulent perturbation field and calculating its statistics remain to be done. Tatarskii approximates the turbulent field as isotropic and homogeneous by using the method of structure functions (Tatarskii, 1961). Accepting that large-scale inhomogeneities may be present, structure functions restore homogeneity by reducing the scale of the analysis.

Standard statistical relations are then applied, resulting in a three-dimensional spectral density function of the form (Tatarskii, 1961),

$$E(K) = A \epsilon^{2/3} K^{-11/3}, \quad (40)$$

where $K^2 = k_x^2 + k_y^2 + k_z^2$, A is a scalar multiplier, and ϵ is the energy dissipation rate.

In the literature (e.g., Duda, et al, 1988), this spectral density has been adapted as follows. To avoid the spectral density becoming infinite at $K = 0$, a wavenumber threshold (outer scale) limit is defined as k_t such that

$$E(K) \approx \frac{1}{(K^2 + k_t^2)^{11/6}}, \quad (41)$$

thus maintaining the $K^{-11/3}$ power law from Tatarskii's spectrum. A highpass filter of the form

$$\frac{K^2}{K^2 + k_t^2} \quad (42)$$

is also added to force the spectral density to zero at $K=0$.

For high wavenumbers, a high-frequency cut-off related to the Batchelor spectrum is given by

$$R_b(K) = \exp \left[-q \left(\frac{K}{K_b} \right)^2 \right], \quad (43)$$

where

$$k_b = \left(\frac{\bar{\epsilon}}{\nu K_T^2} \right)^{1/4} \quad (44)$$

is the Batchelor wavenumber, $\bar{\epsilon}$ is the depth averaged kinetic energy dissipation rate in W/kg, $\nu = 1.40\text{e-}6 \text{ m}^2/\text{s}$ is the kinematic viscosity, and $K_T \approx 1.00\text{e-}7 \text{ m}^2/\text{s}$ is the thermal diffusivity of sea water. The constant q is an order unity factor, and 3.7 is used here in concordance with earlier work (Duda, et al, 1988).

The depth averaged kinetic energy dissipation is defined as (Heney et al, 1986),

$$\bar{\epsilon} = 0.3 \frac{1}{f_I} \left\langle \left[\frac{4}{\pi} j_* N(z) b E_{GM} f_I \right]^2 \cosh^{-1} \left(\frac{N(z)}{f_I} \right) \right\rangle_z. \quad (45)$$

The brackets $\langle \rangle_z$ indicate a depth average, $j_* = 1$ is the characteristic mode for shallow water, $b E_{GM} \approx 0.5m$ is a measure of internal wave intensity, f_I is the inertial frequency in rad/sec, and the buoyancy frequency $N(z)$ may be computed from

$$N(z) = g^{1/2} \left[\frac{1}{\rho(z)} \frac{\partial \rho_p(z)}{\partial z} \right]^{1/2} \text{ (rad/sec)}, \quad (46)$$

where $\rho(z)$ and $\rho_p(z)$ are the density and potential density, respectively, as a function of depth. This expression for $\bar{\epsilon}$ is valid for turbulence created by internal wave decay (Heney et al, 1986). It is an expression developed for deep water and ignores other possible sources of turbulence.

By combining these quantities, the three-dimensional spectral density has the form

$$S_\mu(K) = \frac{\phi_t}{(K^2 + k_t^2)^{11/6}} \frac{K^2}{K^2 + k_t^2} R_B(K). \quad (47)$$

From this expression, the two-dimensional spectral density is calculated below. The integration is applied only to the portion defining the turbulent spectrum (the scaling factor and the wavenumber roll-off terms are added afterwards),

$$\Phi_{3D}(K) = \frac{1}{(K^2 + k_t^2)^{11/6}}. \quad (48)$$

The two-dimensional spectral density is then

$$\begin{aligned} \Phi_{2D}(k_x, k_z) &= \frac{1}{2\pi} \int_{-\infty}^{\infty} \Phi_{3D}(k_x, k_y, k_z) dk_y \\ &= \frac{1}{2\pi} \int_{-\infty}^{\infty} \frac{1}{(k_x^2 + k_y^2 + k_z^2 + k_t^2)^{11/6}} dk_y \end{aligned}$$

$$= \frac{1}{2\pi(k_x^2 + k_z^2 + k_t^2)^{4/3}} \frac{\sqrt{\pi}\Gamma(\frac{4}{3})}{\Gamma(\frac{11}{6})} \quad (49)$$

Employing the same highpass filter, high-wavenumber Batchelor spectrum cutoff, and turbulent strength parameter scaling, the two-dimensional spectral density of turbulent fluctuations of the index of refraction is

$$V_\mu(K) = \frac{\sqrt{\pi}}{2\pi} \frac{\Gamma(\frac{4}{3})}{\Gamma(\frac{11}{6})} \frac{\phi_t}{(K^2 + k_t^2)^{4/3}} \frac{K^2}{K^2 + k_t^2} R_B(K). \quad (50)$$

Note that $V_\mu(K)$ has units of m^3 as expected.

C. IMPLEMENTATION METHODS

1. Numerical Implementation of Turbulence

In the above discussion, $V_\mu(K)$, the two-dimensional spectral density of refractive index perturbations, was related to $\mu(x, z)$, the perturbation field. A random realization of the two-dimensional turbulent field of sound-speed perturbations is obtained by employing the two-dimensional spectrum, $G_\mu(k_x, k_z)$, and defining

$$\mu(x, z) = \frac{1}{(2\pi)^2} \int_{-\infty}^{\infty} \int_{-\infty}^{\infty} [G_\mu(k_x, k_z) B(k_x, k_z) e^{i\theta(k_x, k_z)}] e^{i(k_x x + k_z z)} dk_x dk_z, \quad (51)$$

where $B(k_x, k_z)$ and $\theta(k_x, k_z)$ are two-dimensional random number functions. Since the complex amplitude of each wavenumber component, $B e^{i\theta}$, should exhibit a normal distribution, the random phase of each component is a uniformly distributed random variable on the unit circle. In other words, we define

$$\theta = 2\pi r_1, \quad (52)$$

where r_1 is a uniformly distributed random variable in the interval $[0, 1]$. The magnitude B , however, exhibits a Rayleigh distribution. Because we are in fact generating a realization of the spectral density, we must consider the magnitude-squared, which has a

negative exponential distribution. Thus, the random amplitude of each wavenumber component is obtained by

$$B = \sqrt{-\ln(r_2)}, \quad (53)$$

where r_2 is another independent, uniformly distributed random variable in the interval $[0,1]$.

Since we are implementing this in a model with a discretely sampled grid of the environment, we must consider discrete Fourier transforms computed using an FFT algorithm. Thus, with scaling appropriate to the FFT algorithm being employed,

$$\mu(X_j, Z_k) = \frac{\Delta k_x \Delta k_z}{(2\pi)^2} \sum_{m=1}^M \sum_{n=1}^N \left[G_\mu(k_{xm}, k_{zn}) B(k_{xm}, k_{zn}) e^{i\theta(k_{xm}, k_{zn})} \right] e^{i(k_{xm}x_j - k_{zn}z_k)} \quad (54)$$

From the previous analysis of the relationship between the perturbation spectrum and the spectral density,

$$|G_\mu(k_x, k_z)| = [Area * V_\mu(k_x, k_z)]^{1/2}, \quad (55)$$

where we here define the spectral density up to a scaling factor

$$V_\mu(K) = \frac{\sqrt{\pi}}{2\pi} \frac{\Gamma(\frac{4}{3})}{\Gamma(\frac{11}{6})} \frac{\phi_t}{(K^2 + k_t^2)^{4/3}} \frac{K^2}{K^2 + k_t^2} R_B(K). \quad (56)$$

Note that ϕ_t is the fixed turbulent scaling parameter and may be adjusted to produce the desired RMS perturbation.

Combining the above, we find

$$\begin{aligned} \mu(X_j, Z_k) &= \frac{\Delta k_x \Delta k_z}{(2\pi)^2} \sqrt{Area} \sum_{m=1}^M \sum_{n=1}^N \left[V_\mu^{1/2}(k_{xm}, k_{zn}) B(k_{xm}, k_{zn}) e^{i\theta(k_{xm}, k_{zn})} \right] e^{i(k_{xm}x_j - k_{zn}z_k)} \\ &= \frac{\Delta k_x \Delta k_z}{(2\pi)^2} \sqrt{Area} FFT^{2D} \left[V_\mu^{1/2}(K) B(K) e^{i\theta(K)} \right] \end{aligned} \quad (57)$$

For a given computational area, the factor $Area = RZ$, where the turbulent field exists. Furthermore,

$$\Delta k_x = \frac{2\pi}{R}, \quad \Delta k_z = \frac{2\pi}{Z}, \quad (58)$$

so

$$\Delta k_x \Delta k_y = \frac{(2\pi)^2}{Area}, \quad Area = \frac{(2\pi)^2}{\Delta k_x \Delta k_y}. \quad (59)$$

Thus

$$\mu(X_j, Z_k) = \sqrt{\Delta k_x \Delta k_z} FFT^{2D} \left[V_\mu^{1/2}(K) B(K) e^{i\theta(K)} \right]. \quad (60)$$

Once a realization of $\mu(x, z)$ is computed, we simply multiply by c_o to obtain the sound-speed perturbation,

$$\delta c(x, z) = c_o \mu(x, z). \quad (61)$$

Technically, we might multiply by $c(x, z)$, a sound-speed profile with range. However, variations in $c(x, z)$ are typically less than two percent and so using c_o is a reasonable approximation. Furthermore, note that we are employing the perturbation in cylindrical coordinates, replacing x by r , so

$$\delta c(x, z) \Rightarrow \delta c(r, z). \quad (62)$$

This is also justified so long as we only consider propagation along the two-dimensional slice in (r, z) . See Figure 1 for an example realization of the sound-speed perturbation field.

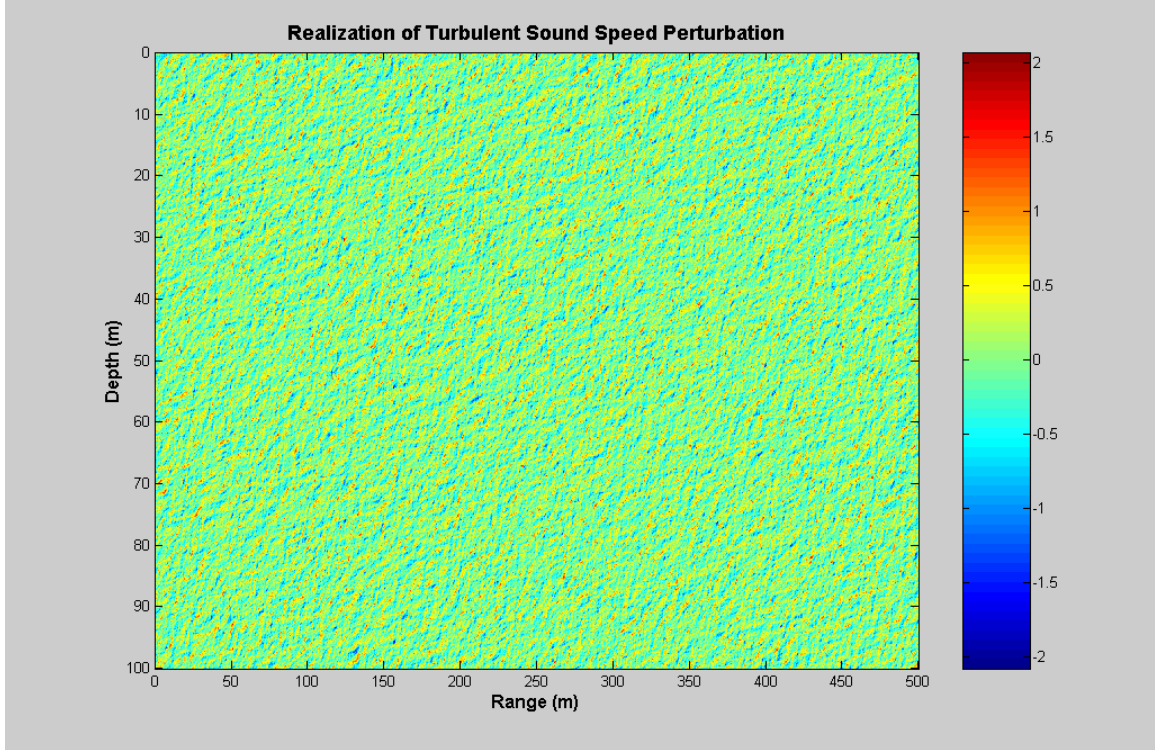


Figure 1. Sample realization of the turbulent sound speed perturbations in m/s. The RMS sound speed fluctuation is 0.41 m/s.

To compute the parameters $A_\mu(z)$ and $\bar{\varepsilon}$, we need to extract both the buoyancy frequency, $N(z)$, and the variance of the temperature gradient, $\left\langle \left(\frac{\partial T'}{\partial z} \right)^2 \right\rangle$. The former may be defined as

$$N(z) = g^{1/2} \left[\frac{1}{\rho(z)} \frac{\partial \rho_p(z)}{\partial z} \right]^{1/2} \text{ (rad/sec)}, \quad (63)$$

where $\rho(z)$ and $\rho_p(z)$ are the depth profiles of the density and potential density, respectively, and g is the acceleration of gravity. Both densities were measured during the ASIAEX experiment by CTD casts.

2. Creation of Source Spectrum

During the experimental periods of interest, characteristic continuous wave (CW) and frequency modulated (FM) pulses were transmitted. The CW pulses of 2 to 3 msec in duration had center frequencies of 4, 8, 16, and 20 kHz. The FM pulses are not analyzed here. To simulate a source pulse of 2 msec, an analysis must be performed in the time domain after the model has run. A band-pass filter of approximately 8 kHz must also be incorporated, to be consistent with the work being done at APL-UW. However, before these concerns can be addressed in detail, a brief summary of time domain processing within the MMPE is necessary.

Recall from the development of the parabolic equation that the time-harmonic acoustic field (ignoring azimuthal dependence) is given by

$$P(r, z, \omega t) = p_\omega(r, z) e^{-i\omega t}. \quad (64)$$

A discrete FFT algorithm is used to represent the field in the time domain as

$$\tilde{P}(r, z, t) = \text{FFT}[p_\omega(r, z)] = \sum_\omega p_\omega(r, z) e^{-i\omega t}. \quad (65)$$

In other words, Eq. (64) represents a single chosen frequency and a single component of the time dependent field. Thus, for analysis in the time domain, the model must be run at multiple frequencies. The inputs required by the model for such analyses are a center frequency (f_c), a bandwidth (BW), and the number of frequency bins to compute (transform size, N). In this research, the bandwidth used was 8184 Hz with a transform size of 1024, consistent with Karpi's previous work.

To view the arrival structure at the receive array ($r = R$, where R is the range of the array from the source), we must compute the complex field $p_{\omega, R}(z)$ for many frequencies and then Fourier transform to obtain $\tilde{P}_R(z, t)$, the complex pressure values in time/depth space. An example $\tilde{P}_R(z, t)$ is shown in Figure 2. Outside the given bandwidth of

$$\left(f_c - \frac{BW}{2} \right) < f < \left(f_c + \frac{BW}{2} \right), \quad (66)$$

the source amplitude is zero. The MMPE model ignores the zeroes outside the bandwidth and computes a base-banded field to avoid unnecessary computations. The resulting expression is

$$\tilde{P}'_R(z, t) = \sum_{\omega} p_{\omega, R}(z) e^{-i(\omega - \omega_c)t}, \quad (67)$$

where $\omega_c = 2\pi f_c$. The complex pressure values $p_{\omega, R}(z)$ are thus placed in frequency bins symmetrically about $\omega - \omega_c = 0$ with limits of $\pm \frac{1}{2}BW$.

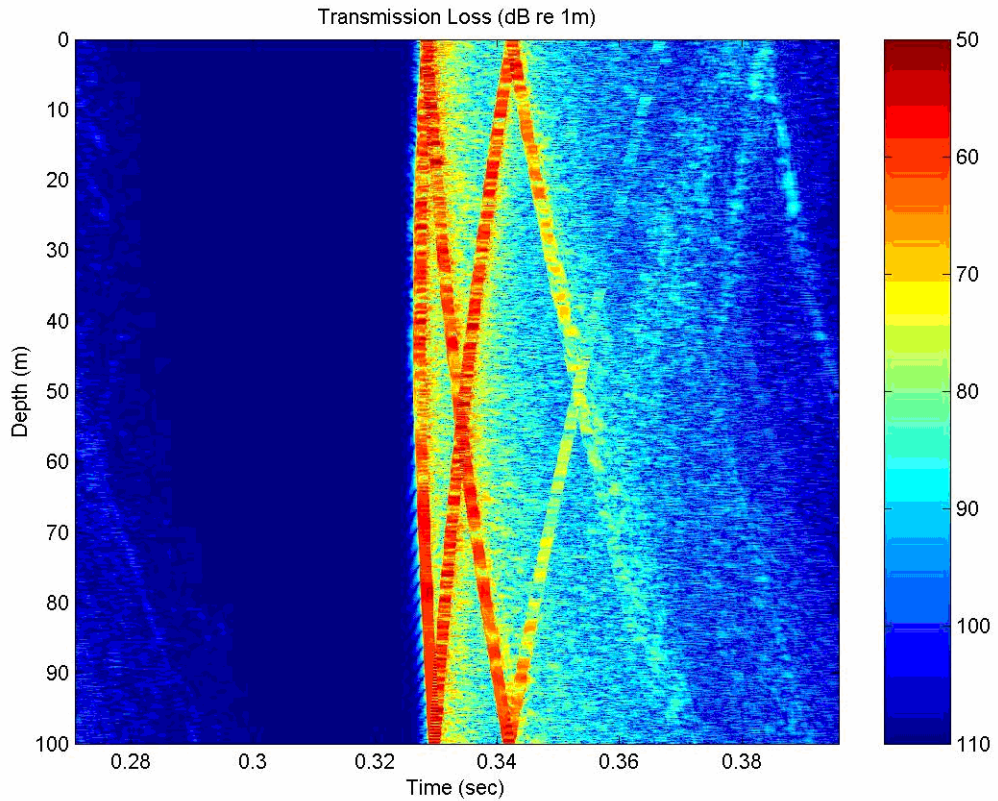


Figure 2. Pulse arrival structure for a source depth of 50m, RMS sound speed perturbation of about 1 m/s, and an outer cutoff length of 10m.

Note the transform pair actually used is

$$\tilde{P}'_R(z, t) \Leftrightarrow \frac{1}{\sqrt{R}} \psi_{\omega, R}(z), \quad (68)$$

where $\psi_{\omega, R}(z)$ is the PE field function and the overall phase factor $e^{ik_0 r} = e^{i\omega R/c_0}$ is neglected. As a result, arrival times are given as values of “reduced time”, τ , such that

$$\tau = \left(t - \frac{R}{c_0} \right), \quad (69)$$

where c_0 is the reference sound speed. The complex pressure values $\tilde{P}'_R(z, t)$ are thus placed in time bins symmetrically about $\tau = 0$, with limits of $\pm \frac{1}{2}T$, where T is the total length of the time window. The time step is given by

$$\Delta t = \frac{1}{BW} \approx .122 \text{ msec}, \quad (70)$$

with a corresponding frequency step of

$$\Delta f = \frac{BW}{N-1} = \frac{8184 \text{ Hz}}{1024-1} = 8 \text{ Hz}. \quad (71)$$

Running the model at multiple frequencies has thus enabled the analysis of the time dependent field.

The APL team from the University of Washington attempted to remove some of the out-of-band noise from the ASIAEX data by applying a digital band-pass filter to the signal. During the filtering process, they preserved 8 kHz of bandwidth, using roughly a ± 4 kHz band around the center frequency. However, the band-pass filter was not always applied symmetrically about the center frequency of the signal. In order for the model’s results to be comparable, the model was run using a center frequency defined by the center of the filter. For example, on a model run meant to simulate a 2 msec pulse at 20 kHz, a center frequency of 19 kHz was input to the model, corresponding to the center of the filter. Thus, the output data is centered properly, but still representative of a continuous source.

To simulate a 2 msec pulse, a filter function was applied to the data. A square filter function (shown below in Figure 3) was chosen to represent the pulse in the time domain. The length of the filter corresponds to the number of discrete time steps that are needed to comprise the pulse, found by

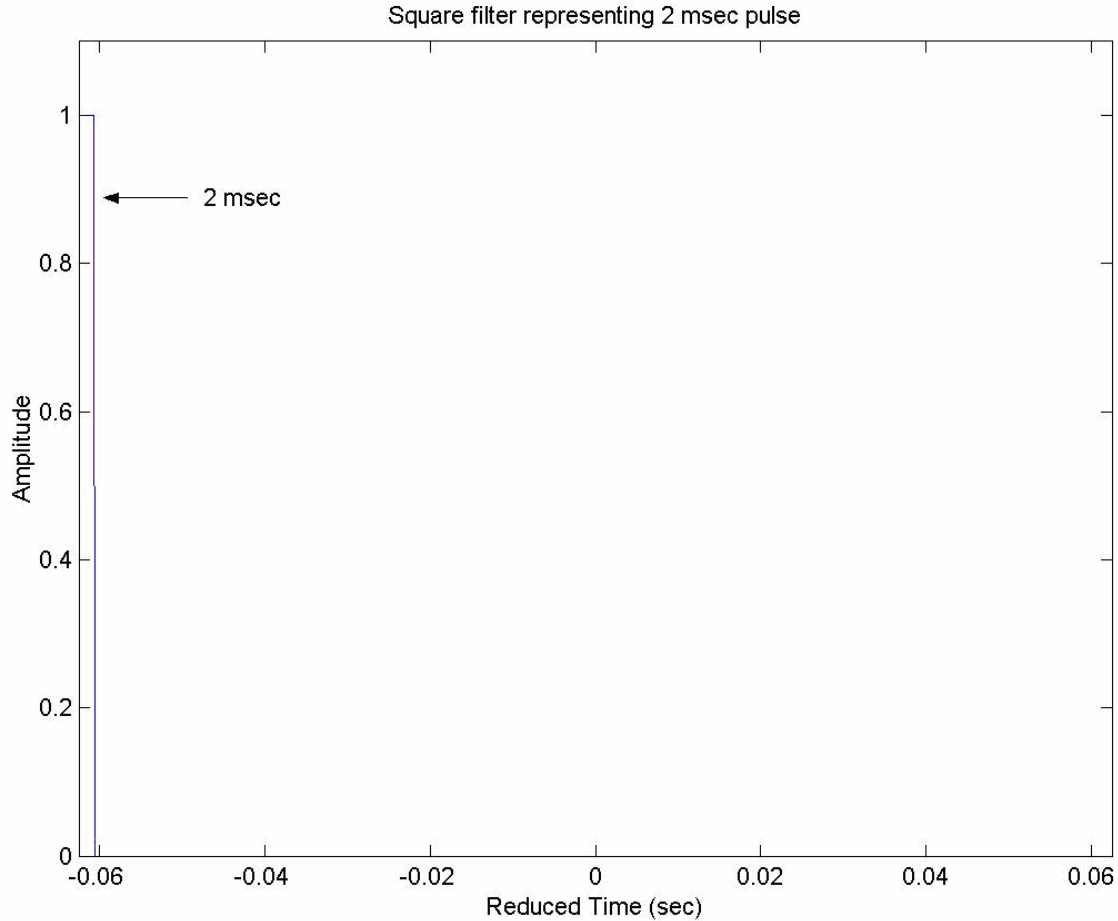


Figure 3. Square filter function representing a 2 msec pulse.

$$n_{pulse} = \frac{2\text{msec}}{\Delta t} = 16, \quad (72)$$

where the time step is 0.122 msec, as shown in Eq. (70). This square filter will then be transformed to a source spectrum in the frequency domain, as shown in Figure 4, and

applied to the output data. However, the output data is centered at the middle of the bandpass filter, and the source spectrum should be applied at the center frequency of the source. Thus, a shift may be required. In the above example, a shift of 1 kHz would be needed to center the source spectrum at 20 kHz instead of 19 kHz. Table 1 provides a list of the filters used and the corresponding shift required.

Experimental Carrier Freq. (kHz)	Minimum Freq. of Filter (kHz)	Maximum Freq. of Filter (kHz)	Center Freq. of Filter (kHz)	Required Shift (kHz)
4	2	10	6	2
8	5.5	13.5	9.5	1.5
16	12	20	16	0
20	15	23	19	1

Table 1. Characteristics of the bandpass filters used in data processing for each experimental carrier frequency. The required shift is the difference between the center of the filter and the experimental carrier frequency.

To allow for shifting, the generated source spectrum must have a wider bandwidth (BW) than the output data. The bandwidth is simply doubled, resulting in a new time step, $\Delta t'$, given by

$$\Delta t' = \frac{1}{BW'} = \frac{1}{2BW} \approx 0.061\text{msec}, \quad (73)$$

and thus twice as many steps are required for a 2 msec pulse,

$$n_{pulse}' = \frac{2\text{msec}}{\Delta t'} = 32. \quad (74)$$

Note that the total time window T and the frequency step Δf remain constant. The end result is an identical spectrum with more frequency information added on each side to make the spectrum twice as long. The original spectrum can be seen below in Figure 4 and Figure 6 illustrates the extended version.

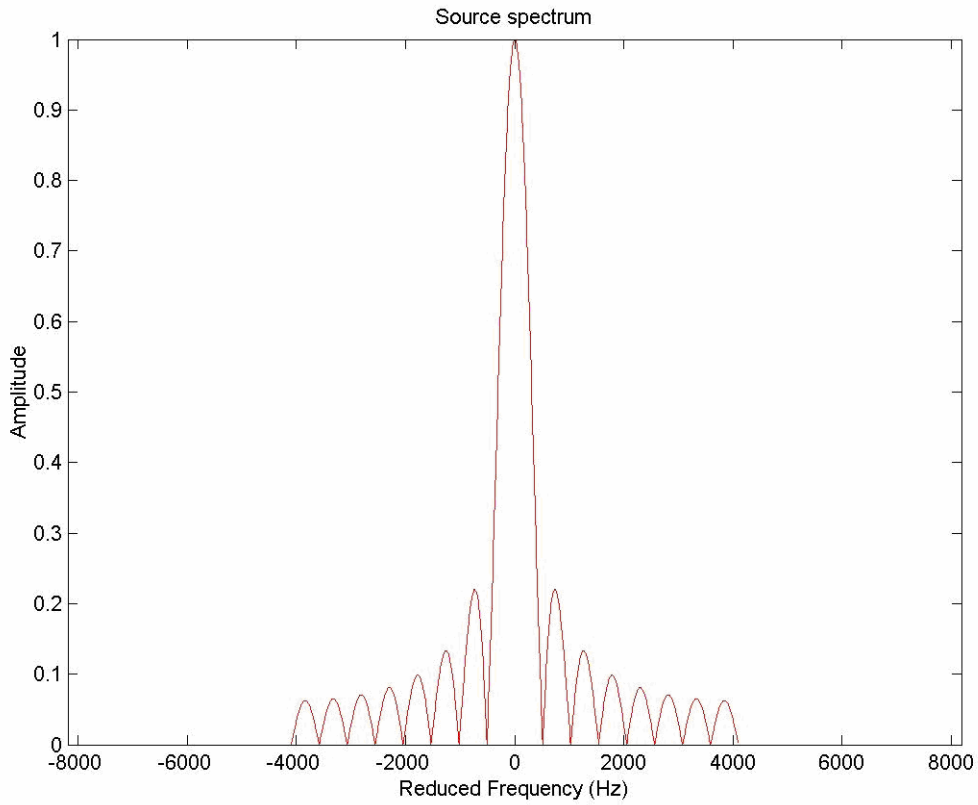


Figure 4. Source spectrum created from 2 msec square window with a bandwidth of 8184 Hz.

In the frequency domain, the square window takes the expected sinc function form, given by

$$\text{sinc}(x) = \frac{\sin(x)}{x}. \quad (75)$$

The source spectrum developed above must now be combined with an appropriate band-pass filter. A rectangular window with a Hanning taper at each end was chosen for this purpose. The Hanning window that was used can be defined as

$$w[k] = \frac{1}{2} \left(1 - \cos \left(2\pi \frac{k}{n+1} \right) \right), \text{ where } k = 1, \dots, n. \quad (76)$$

The shape of a Hanning window can be seen in Figure 5. The Hanning window was subsequently divided into halves, each half being applied to an end of the rectangular window, and the total filter width being equal to 8 kHz in this case (spanning 15-23 kHz).

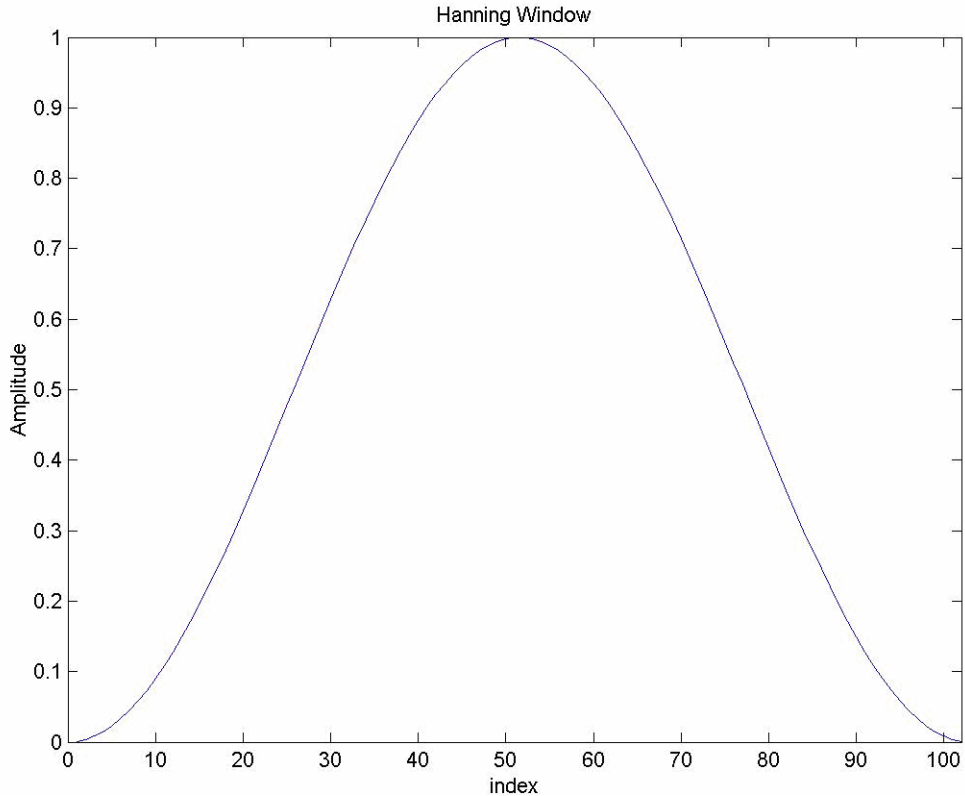


Figure 5. Typical Hanning Signal-Processing Window

This system response filter was then used as a multiplier on the 2 msec pulse spectrum, thus completing the source amplitude function. An example bandpass filter and source spectrum are shown together in Figure 6 for a carrier frequency of 20 kHz.

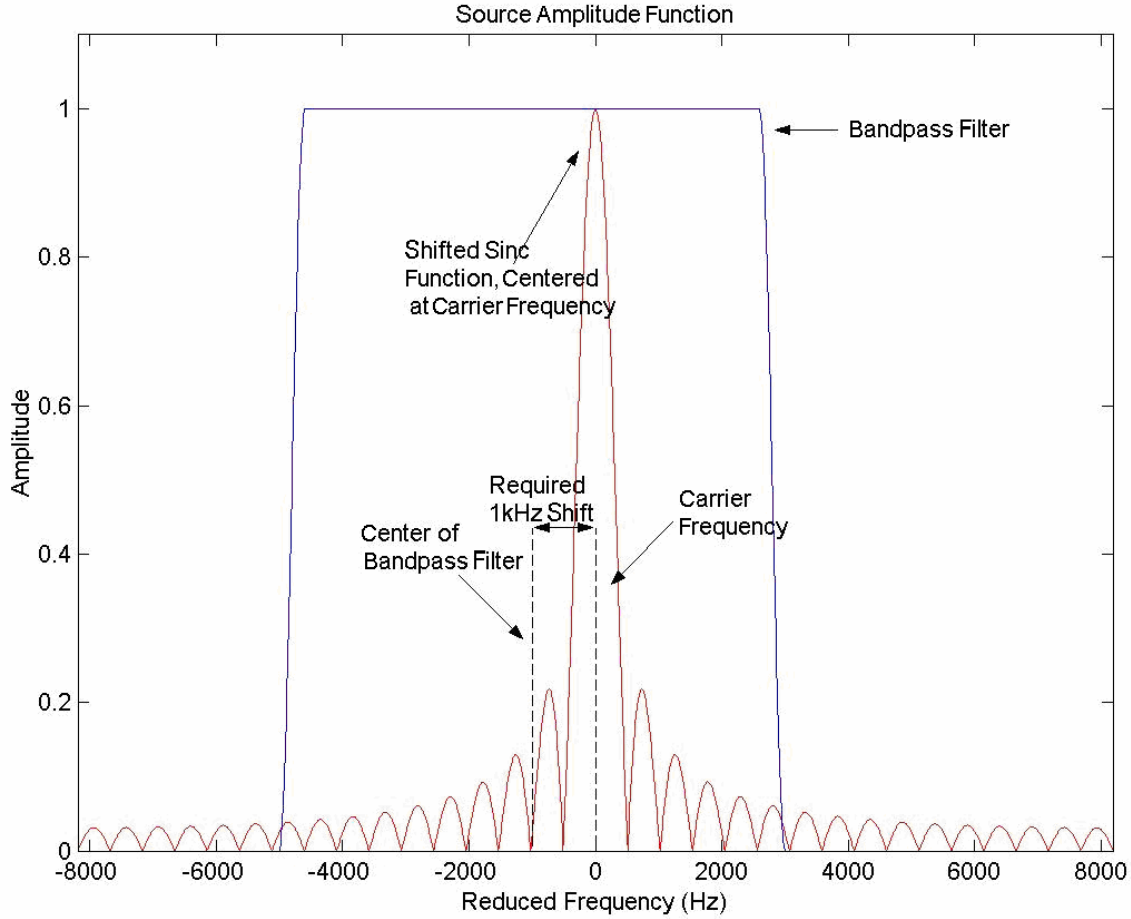


Figure 6. Extended source spectrum overlaid with 8 kHz bandpass filter. In this case, a carrier frequency of 20 kHz is used, thus requiring a 1 kHz shift.

3. Direct Path Extraction

At the boundaries of the medium, the acoustic signal interacts with the surface of the water and the iso-speed bottom (set at 1600m/s). In order to remove the interface effects from the analysis and focus strictly on the volume effects, the direct path arrival was extracted. As can be seen in Figure 7, for a source depth of 50 meters, several propagation paths are evident in the pressure time series (received at 500m range).

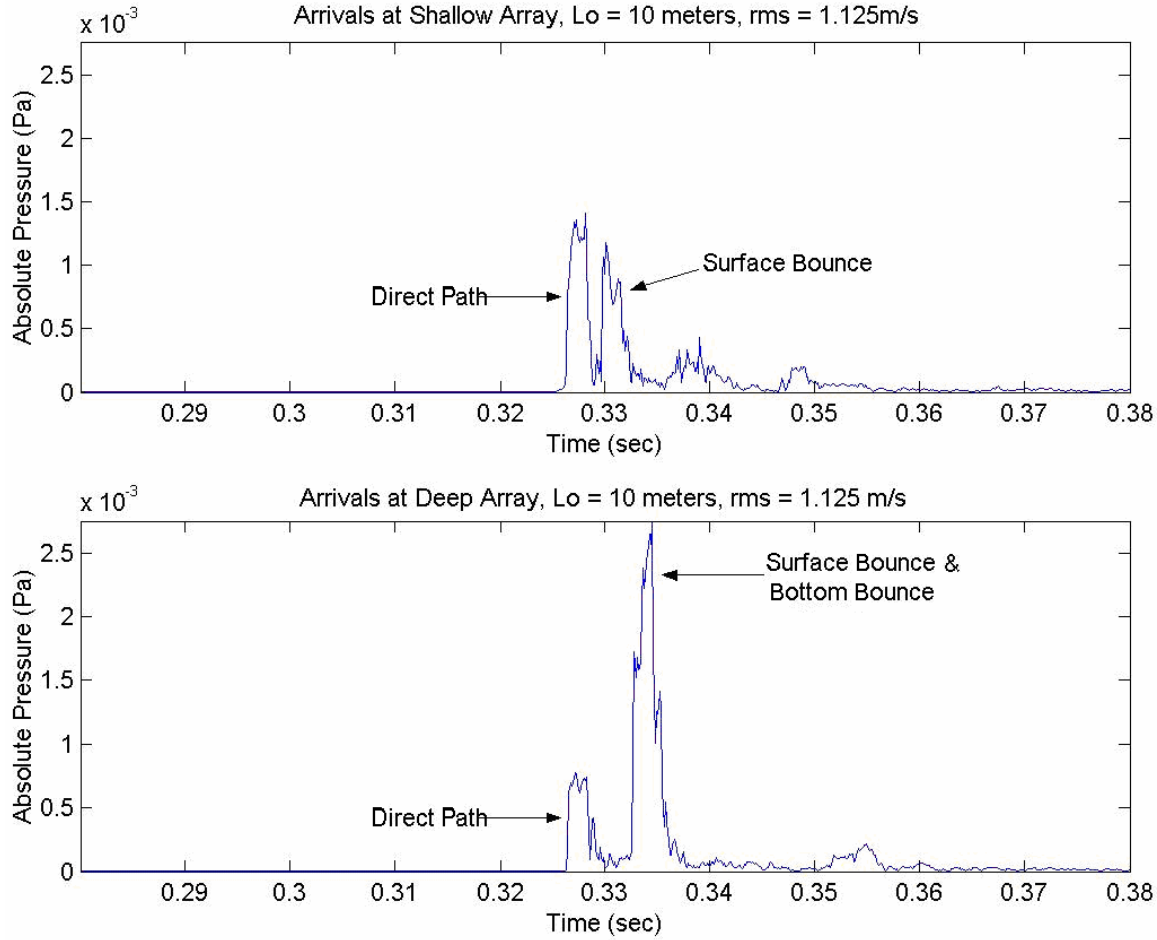


Figure 7. Pressure time series received at shallow and deep depths at a range of 500 meters. Lo is the outer cutoff length, and RMS is the RMS value of the sound speed perturbation.

A source depth of 25 meters in some cases results in a direct path signal indistinguishable from the surface bounce arrival. As in earlier research by Karpi, a 50-meter source depth will be considered as a reference. Plots similar to Figure 7 were analyzed for each model run to determine the times encompassing the direct path arrival. The time series was then extracted directly, without filtering, as shown in Figure 8. The direct path extraction is performed at six varying depths across each of the roughly 5 m length vertical array clusters. The uppermost depths of each sub-array were defined as the numerical mesh points closest to 35, 45, 55, and 65 m. The depths of the five lower elements were then approximately 15, 45, 105, 225, 465 cm below the uppermost

element, thus spanning roughly 5 m. Therefore, 24 total signals are extracted, one for each of the six elements in the four sub-arrays.

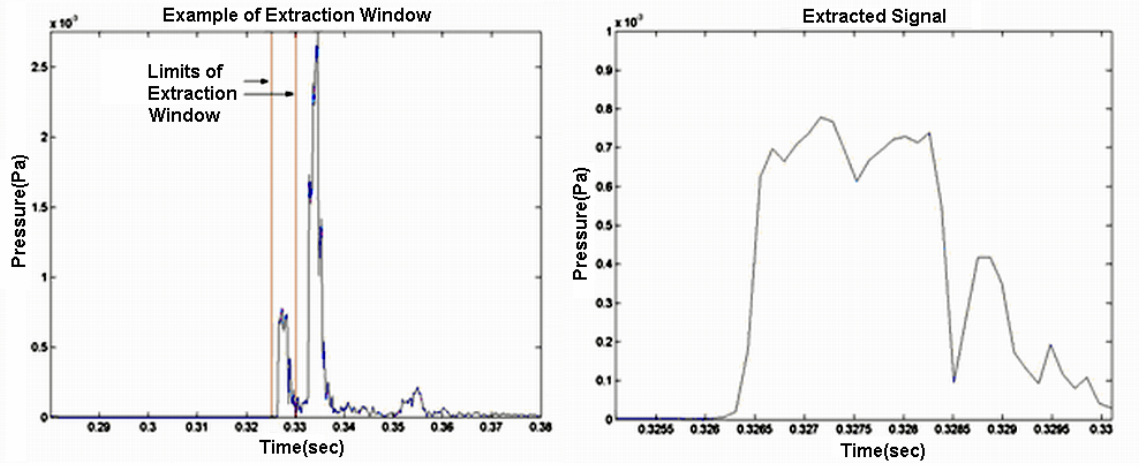


Figure 8. Extraction of the Direct Path Arrival.

4. Vertical Spatial Correlation

It is now possible to obtain a quantitative estimate of signal degradation by cross-correlating the extracted direct path signals. Correlation is a measure of the similarity between two waveforms. In this case, signals recorded at different depths along the same propagating wavefront are compared. If signal degradation was not present, such as when propagating through a homogeneous medium, we would expect the received pressure signal to be very similar at different points along the front. As the similarity of the received signals along the front decreases due to inhomogeneities, we say that our wavefront has degraded.

In the experiment, each of the six elements in a vertical array cluster has a corresponding received pressure signal recorded at the depth of the element. Thus, 15 different cross-correlations are possible (element 1 with element 2, element 2 with element 3 and so forth), in addition to the auto-correlation, each with a depth separation given by the separation of the elements being correlated. The final output is a graph of the normalized maximum vertical cross-correlation as a function of the depth difference

of the elements being correlated with 16 points. These 16 points include each possible combination between elements and the autocorrelation of the signal at element one.

Practically, each extracted direct path signal is cross-correlated using the MATLAB function *xcorr*, which generates one number for the normalized max correlation. Note that “normalized” means the autocorrelation (the correlation of the signal with itself) is assigned a value of 1. The normalized cross-correlation can be represented as follows:

$$C_{p_1, p_2}(\tau) = e^{-i2\pi f_c \tau} \frac{\int p_1'(T) p_2'^*(T - \tau) dT}{\sqrt{\int |p_1'(T)|^2 dT \int |p_2'(T)|^2 dT}}, \quad (77)$$

where p_1' and $p_2'^*$ are the first base-banded pressure signal and the complex conjugate of the second base-banded pressure signal, respectively.

III. MODEL VARIABLES

A. EXPERIMENTAL AND MODEL GEOMETRY

The input parameters to the MMPE model were taken mostly from data sets of the East China Sea experiment, and the geometry and source characteristics were modeled after the short-range experiment conducted by the group from APL-UW. The horizontal range between the source, placed at a depth of either 25 or 50 m, and receivers was set at 500 m, and the water column depth was set at 100 m. In the ASIAEX experiment, two four-element vertical arrays were placed at nominal depths of 26 and 52 m. The distances between the elements of each array were 13, 30, and 60 cm. Figure 9 below shows the experimental configuration.

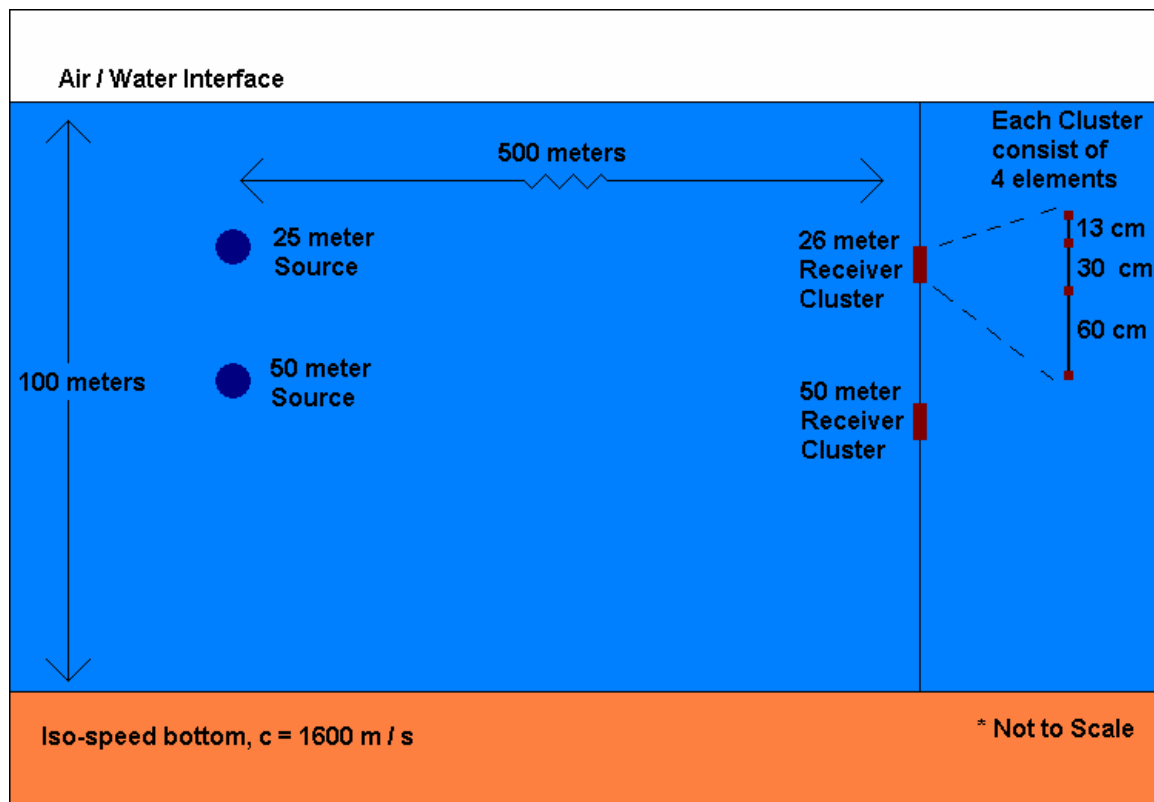


Figure 9. Experimental Geometry from ASIAEX

The MMPE model is capable of incorporating both shallow and deep bottom characteristics. In this work, however, the deep bottom depth was set at 3000 m, deep enough not to affect propagation. The sound speed of the shallow bottom was set at a constant of 1600 m/s. This version of the MMPE model requires a reference sound speed, c_0 , set at 1500 m/s for this research. It should also be noted that all results presented here are for runs done in “efficiency” mode as opposed to “accuracy” mode. The difference between the two modes is in mesh size, Δr , Δz . Efficiency mode was chosen because it is much faster than accuracy mode, and in most cases should be accurate enough for our direct path analysis.

Though this research is mostly concerned with the effects of environmental variables, it is also a point of interest to learn about the effects of the geometric variables, such as source and receiver depths. Since the model computes the solution at all computational depth grid points, it is a simple matter to analyze the dependence of signal coherence on receiver depth. Thus, the numerical work presented here differs in geometry from ASIAEX in that a total number of four receiver sub-arrays with six elements each are processed. All analysis in this work used uppermost sub-array element depths of 35, 45, 55, and 65 m, with total apertures of roughly 5 m.

1. Source Depth

In contrast to the ASIAEX geometry, the influence of five different source depths is examined in this research. A depth of 50 m is assumed as the reference source depth. Other source depths included 30, 40, 60, and 70 m. The reference geometry for the 50 m source depth and the four sub-arrays is displayed in Figure 10.

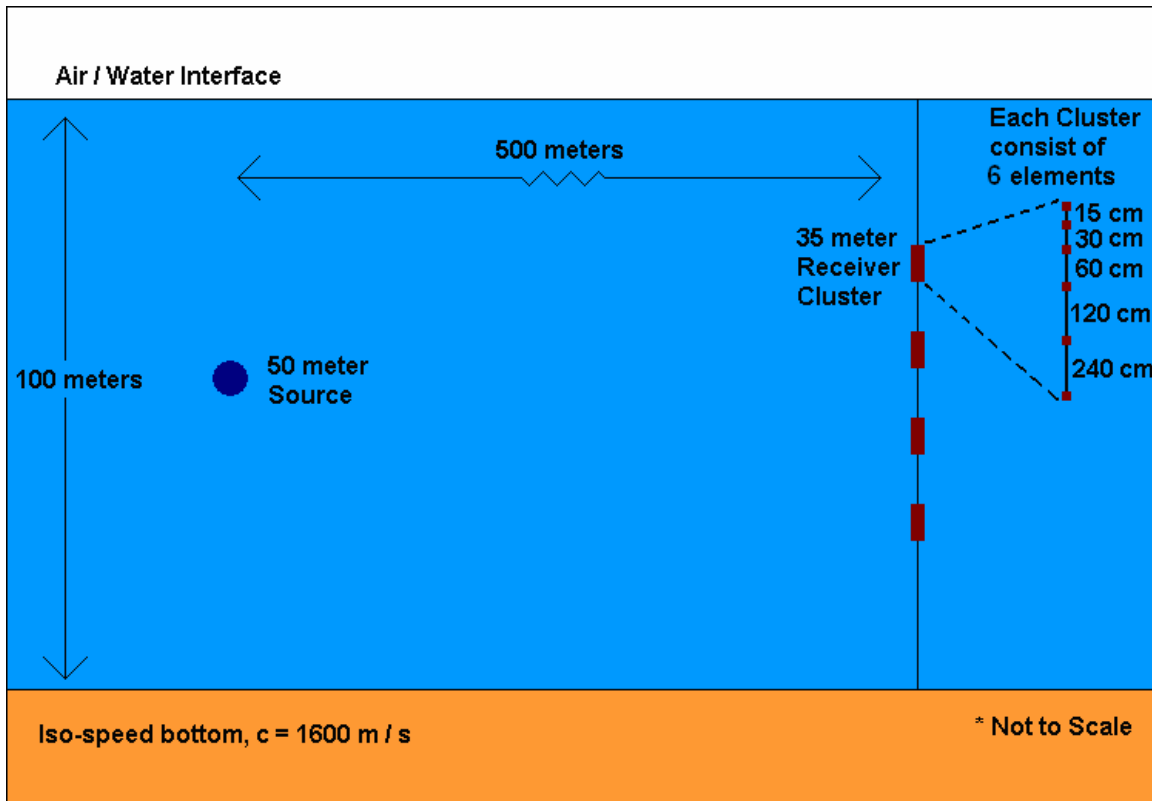


Figure 10. Model Geometry Used in This Research

B. ENVIRONMENTAL MODELS

The focus of this research is on the influence of turbulence, so parameters associated with the description of the turbulent field will be varied to determine their influence. Specifically, we will examine the effect of variable outer length cut-off scale, k_t , and overall turbulent strength scaling parameter, ϕ_t . These parameters have a direct effect on the structure of the turbulence, and thus a direct effect on the coherence of the propagation. In addition to these parameters, we shall also examine how source/receiver geometry, which affects propagation path, may influence the signal coherence. Since the propagation paths are related to the background sound speed profile, analysis will also be performed with other SSPs.

1. Turbulence Strength

As noted in Chapter II, the spectral density of turbulence, given by Eq. (65), has an overall scaling factor, ϕ_t , which we refer to as the turbulent scaling parameter. Any desired RMS perturbation may be obtained by adjusting this scaling parameter. In this work, the turbulent scaling parameter has been fixed at five specific values, considered to range over realistic turbulence perturbation scales from very weak to very strong. One value was considered a reference value, two values were examined below reference, Ref-1 and Ref-2, and two values were examined above reference, Ref+1 and Ref+2. Sample values for the RMS perturbation for each of the turbulent strength cases is provided in Table 2.

Case	Ref-2	Ref-1	Reference	Ref+1	Ref+2
RMS	0.112	0.224	0.448	0.897	1.793

Table 2. RMS Perturbation of Sound Speed (m/s) for Different Turbulent Strengths

2. Turbulence Outer Length Scale

The outer length cutoff scale, k_t , in Eq. (65) serves as a low wavenumber cutoff, limiting contributions from the turbulent perturbation to wavenumber values roughly greater than k_t . Since

$$k_t = \frac{2\pi}{\lambda_t}, \quad (78)$$

then λ_t is a wavelength threshold that limits the spatial scale of the turbulent fluctuations.

The weak scattering theory dictates that the scattering of a propagating signal results mainly from perturbations on the scale of the Fresnel radius. The Fresnel radius, R_f , is given by (Duda et al, 1998)

$$R_f = \sqrt{r\lambda}, \quad (79)$$

where r is the transmission range and λ is the wavelength of the signal. For a signal with a frequency of 4 kHz, the wavelength is given by

$$\lambda = \frac{c_0}{f} = \frac{1500m/sec}{4000Hz} = 0.375 m . \quad (80)$$

Thus for a transmission range of 500 m, the Fresnel radius is

$$R_{f,500m,16kHz} = \sqrt{500m * 0.375m} \approx 13.7m . \quad (81)$$

The corresponding “Fresnel wavenumber” is then about $0.46 m^{-1}$. Table 3 shows the Fresnel radius and Fresnel wavenumber values for frequencies examined in this research.

Frequency (kHz)	Wavelength (m)	Fresnel Radius (m)	Fresnel Wavenumber (1/m)
4	0.375	13.693	0.459
8	0.188	9.682	0.649
16	0.094	6.847	0.918
20	0.075	6.124	1.026

Table 3. Fresnel Radius and Fresnel Wavenumber Values for Different Frequencies at a Range of 500 m

Though the values for the Fresnel radius vary between 6 and 14 m, 10 m is used as the reference case for the turbulence outer length scale for all frequencies in the research. The other values examined in this work are 2 m and 5 m, as Ref-2 and Ref-1, respectively, and 25 m and 50 m, as Ref+1 and Ref+2, respectively. As the scale value was increased from low values, the most distinguishable change occurred around 10 m, which is in the vicinity of the Fresnel radius. So the Fresnel radius may be considered as a critical threshold for the values of outer scale regarding the disturbance of a signal by turbulence. In other words, since we assumed 10 m as the reference value for the turbulence outer length scale, the correlation curves should begin to exhibit a decorrelation at this value. As we increase this scale parameter to values greater than the Fresnel radius, then the correlation curves may change slightly. But as we decrease this parameter to values less than the Fresnel radius, a dramatic change in coherence should occur, and the correlation should increase considerably.

Figures 12 to 14 show one-dimensional slices of the turbulent perturbation energy density spectrums in the wavenumber domain for different outer length scales. It is important to note that around 2 m^{-1} , the amplitudes of the spectra are very similar.

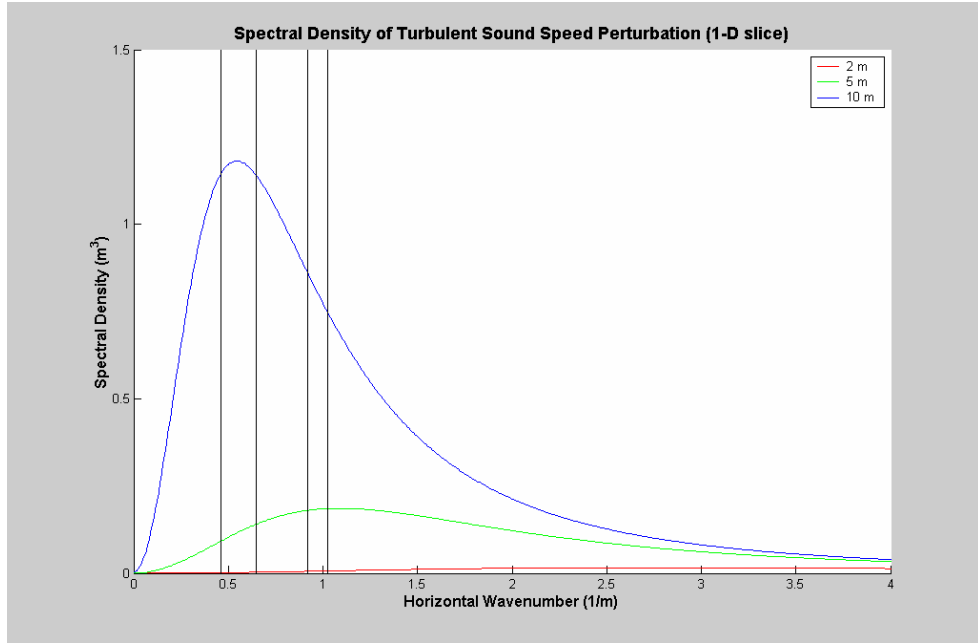


Figure 12. One-dimensional energy density spectra for reference outer length scale (10 m) and values below (2m and 5m). Vertical lines are the Fresnel radius values for 4, 8, 16, and 20 kHz, from left to right, respectively.

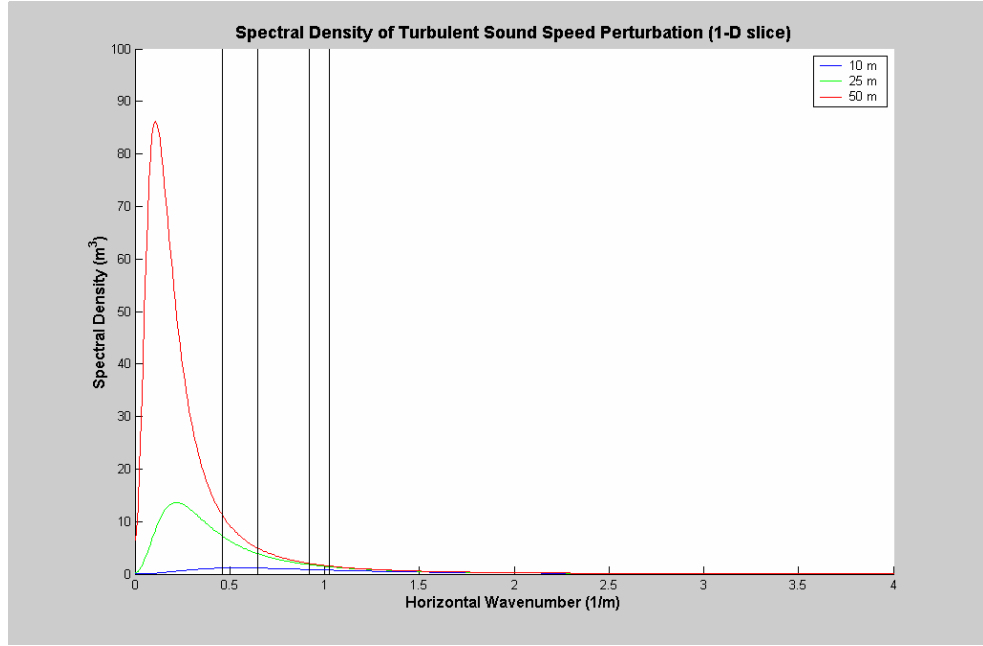


Figure 13. One-dimensional energy density spectra for reference outer length scale (10 m) and values above (25m and 50m). Vertical lines are the Fresnel radius values for 4, 8, 16, and 20 kHz, from left to right, respectively.

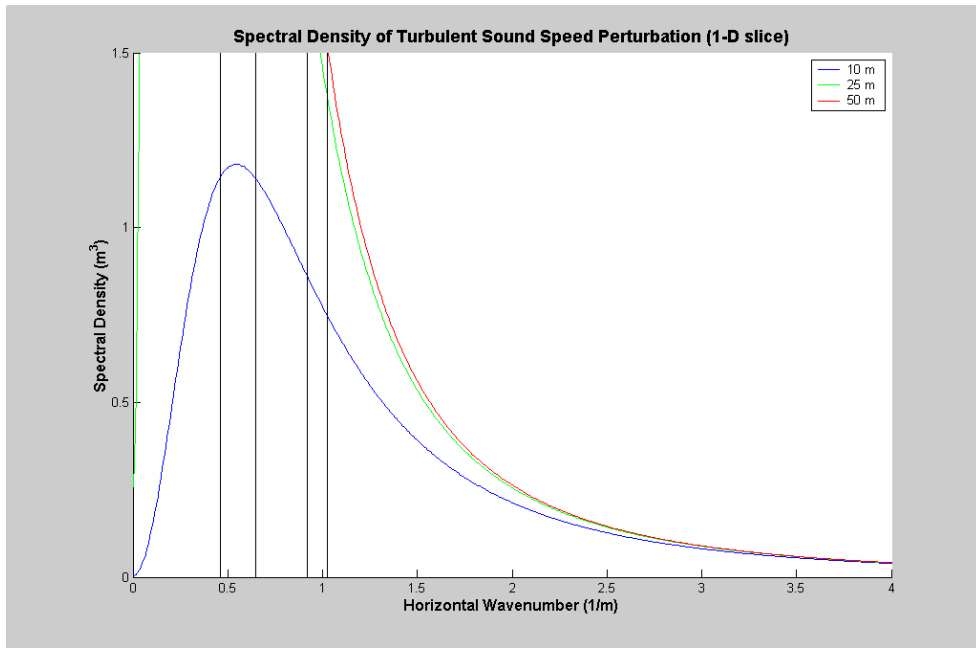


Figure 14. One-dimensional energy density spectra for reference outer length scale (10 m) and values above (25m and 50m) on a smaller scale. Vertical lines are the Fresnel radius values for 4, 8, 16, and 20 kHz, from left to right, respectively.

Another important point to make about the influence of the turbulent outer length scale is that changing this value changes the RMS sound speed perturbation value. For the reference turbulent strength scaling, sample RMS values for the five different outer length cut-off scales are shown in Table 4.

Case	Ref-2	Ref-1	Reference	Ref+1	Ref+2
RMS	0.217	0.338	0.448	0.627	0.799

Table 4. RMS Perturbation of Sound Speed (m/s) for Different Cases of Turbulence Outer Length Scale Parameter

3. Sound Speed Profiles

During the ASIAEX, 54 CTD casts were made by the Chinese research vessel *Shiyan-3* from 2 to 6 June, 2001. The reference SSP is taken as the average value of these measurements. In addition to the reference sound speed profile, three other individual sound speed profiles were examined in this analysis. One was chosen as being reasonably close to the mean (reference) profile, one was chosen as being the most deviated from mean with a deeper thermocline, and the third was chosen as being the most deviated from mean with the uppermost thermocline. These three profiles are referred to as Closest to Mean (CTM), Most Deviated Down (MDD), and Most Deviated Up (MDU), respectively. Figure 11 shows how the four sound speed profiles compare.

Analysis of the influence of background sound speed profile is more complex than the other environmental parameters because the variability introduced in the signal coherence is not easily predictable. Indeed, we initially assumed that the background profile would not significantly affect such short range coherence results. The analysis presented in the following chapter, however, does indicate a significant dependence on the background profile and the propagation path geometry.

Previous work by Duda and Bowlin (1994) examined the influence of sound speed relative curvature on signal stability. However, this approach was examined in the context of long-range, deep-ocean environments and assumed to hold for multi-cycle ray

propagation. Therefore, it is unclear if a similar measure of the background sound speed profiles in this environment will relate in any way to signal coherence along specific ray path geometries.

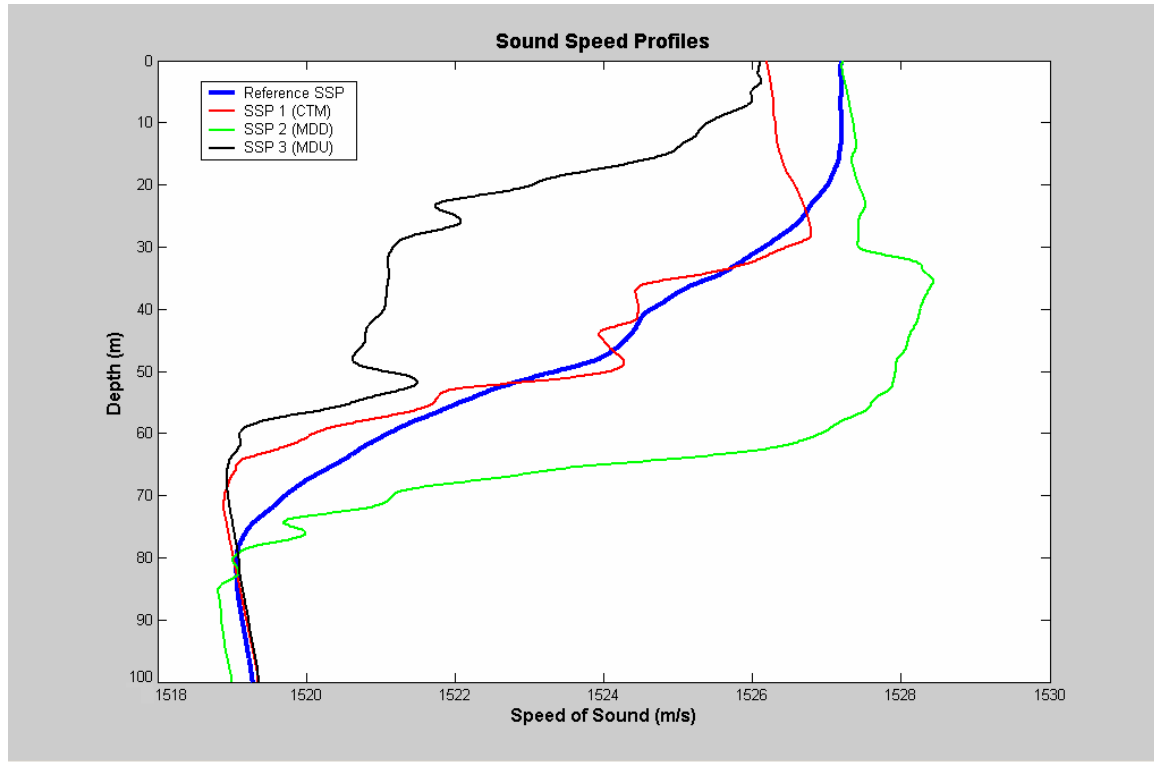


Figure 11. Sound Speed Profiles Used in the Modeling Analysis

THIS PAGE INTENTIONALLY LEFT BLANK

IV. POST PROCESSING AND ANALYSIS

As explained in Chapter II, the vertical spatial correlation is used to examine the signal degradation. If signal degradation is not present, then the correlation is going to be very close to unity. A perfect correlation value of 1 is the expected result of an autocorrelation (the correlation of the signal with itself). All other combinations for correlation are normalized according to the autocorrelation result, and thus they are less than or equal to 1.

The correlations are calculated as a function of the “depth difference/wavelength.” The center frequency of the signal and $c_0 = 1500 \text{ m/s}$ are used for the wavelength estimation.

For each parameter, the reference case is shown first followed by the various results for other values of that parameter. Therefore, some figures are included several times to allow for convenient comparison. “Reference Case” means that all parameters are adjusted to their reference values.

During the analysis of the turbulence outer length scale, sound speed profile, and source depth parameters, the reference turbulence strength didn’t create enough variability for 4 kHz and 8 kHz. Therefore, during the analysis of these parameters, the reference scale for these frequencies is changed. Specifically, the Ref+2 turbulence strength parameter is used for the 4 kHz analysis, and the Ref+1 turbulence strength parameter is used for 8 kHz analysis. All graphs exhibit four different correlation plots for the different receiver sub-arrays, with the uppermost plot corresponding to the shallowest sub-array and the lowermost corresponding to the deepest.

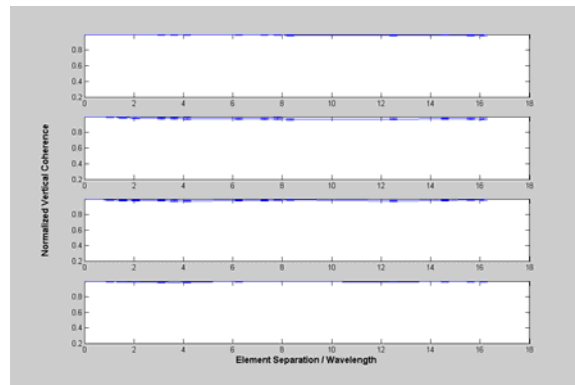
A. TURBULENCE STRENGTH

The turbulence strength is a parameter that directly affects the scale of turbulence in the environment. As expected, the influence of this parameter is found to depend upon frequency of the propagation. Examining Figures 15 through 18, it can be easily seen that

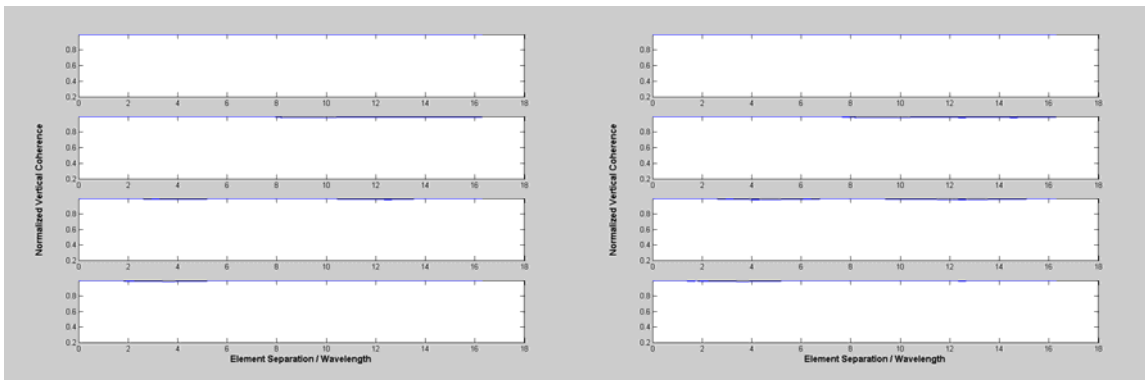
as the frequency is increased, the same turbulence strength produces significantly more variability in the propagation. This effect is most noticeable when the frequency is doubled (from 4 kHz to 8 kHz, then 8 kHz to 16 kHz), but is not as evident above 16 kHz in this analysis. Figures 17 and 18 show that 20 kHz propagation has almost the same vertical coherence as 16 kHz.

Another important result to note is that the coherence for the deepest sub-array is a lot higher than the other sub-arrays for almost all cases of varying frequency or strength parameter. This may be related to the background sound speed profile with which the acoustic path interacts. This will be examined further in a subsequent section using a simple ray tracing model.

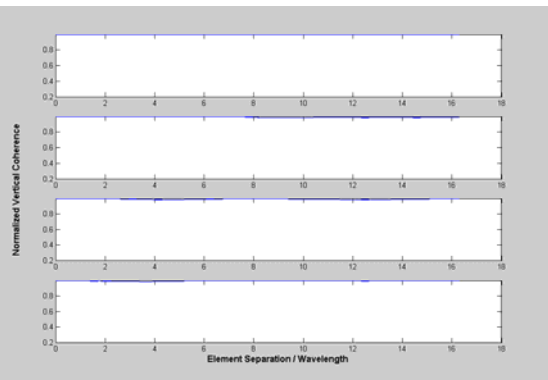
Also note that these figures indicate little effect of the turbulence at 4 kHz when the reference strength parameter is employed. As previously noted, all subsequent analysis at 4 kHz will be performed using the highest (Ref+2) turbulence strength parameter. Similarly at 8 kHz, all subsequent analysis will be performed using the second highest (Ref+1) turbulence strength parameter.



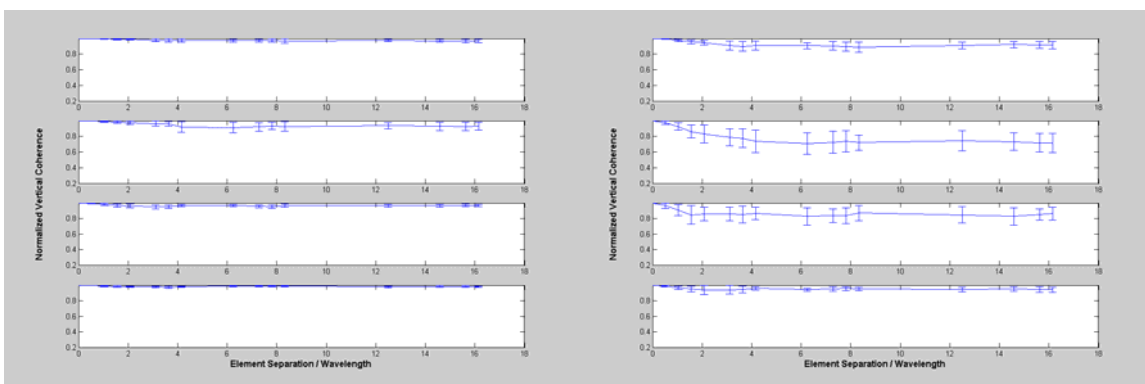
(a)



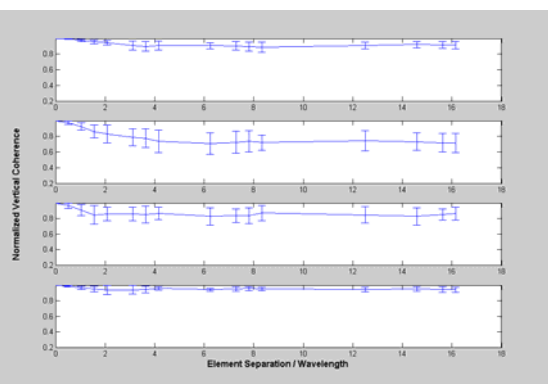
(b)



(c)



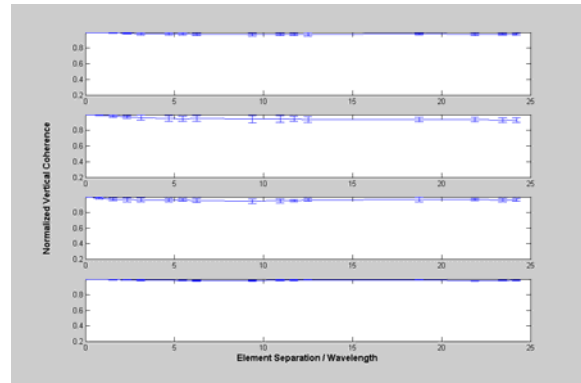
(d)



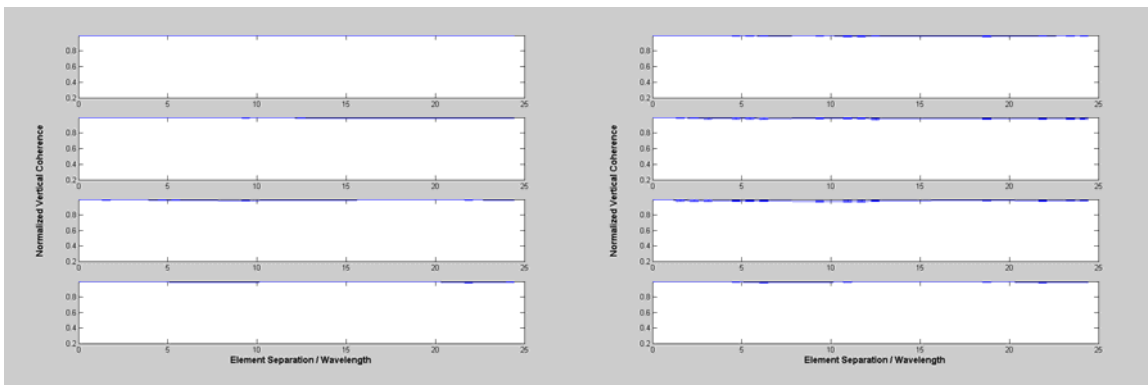
(e)

Figure 15. Effect of Turbulence Strength Parameter at 4 kHz.

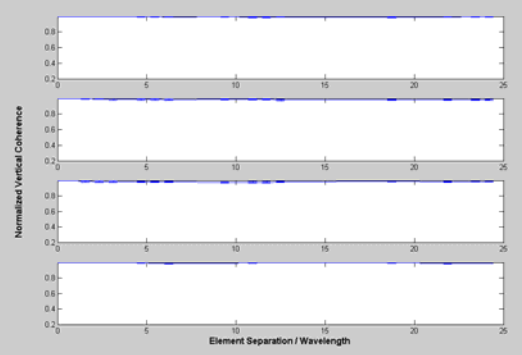
(a) Turbulence Strength = Reference, (b) Turbulence Strength = Ref-2, (c) Turbulence Strength = Ref-1, (d) Turbulence Strength = Ref+1, (e) Turbulence Strength = Ref+2



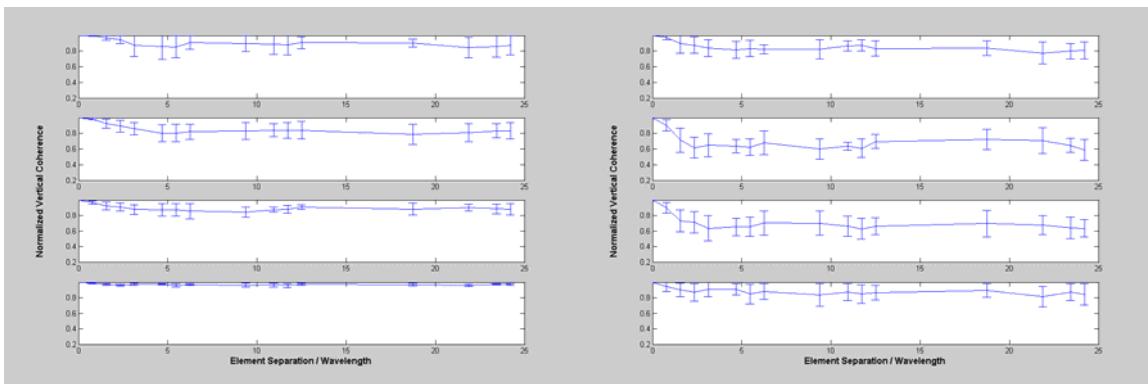
(a)



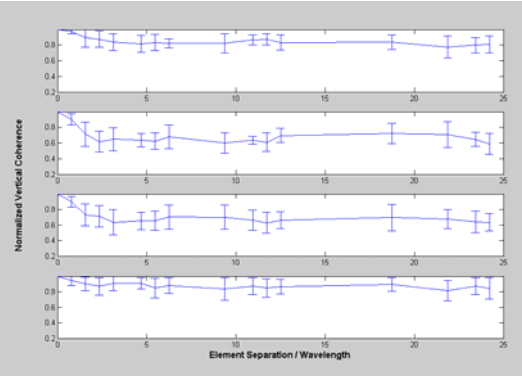
(b)



(c)



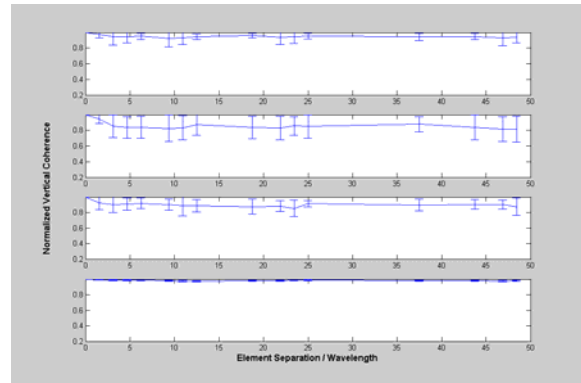
(d)



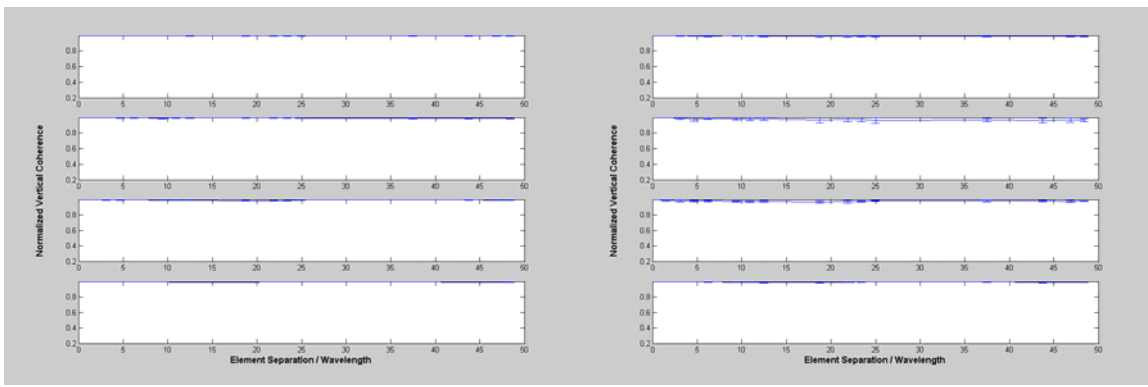
(e)

Figure 16. Effect of Turbulence Strength Parameter at 8 kHz.

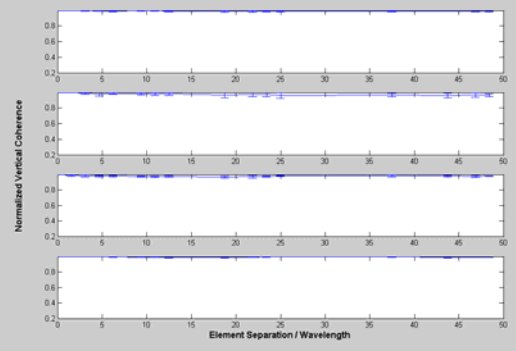
(a) Turbulence Strength = Reference, (b) Turbulence Strength = Ref-2, (c) Turbulence Strength = Ref-1, (d) Turbulence Strength = Ref+1, (e) Turbulence Strength = Ref+2



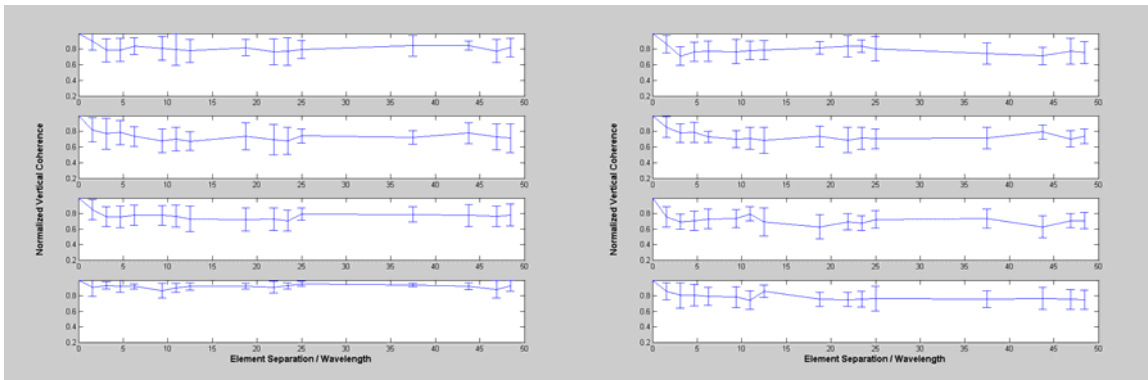
(a)



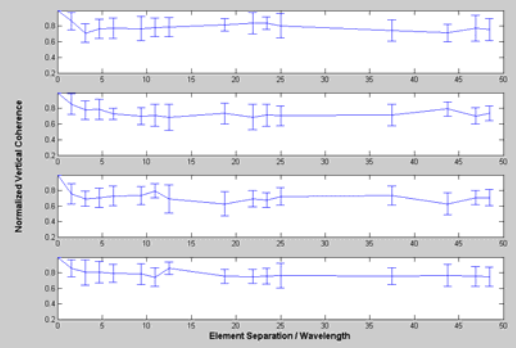
(b)



(c)



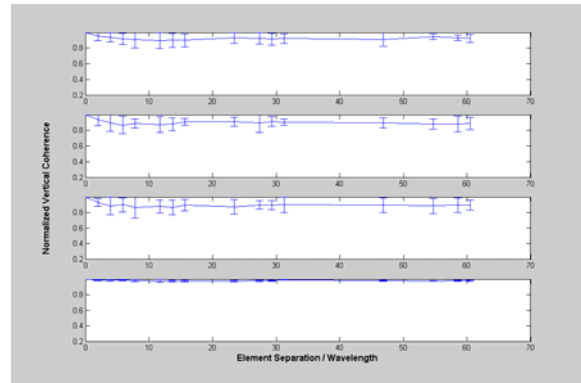
(d)



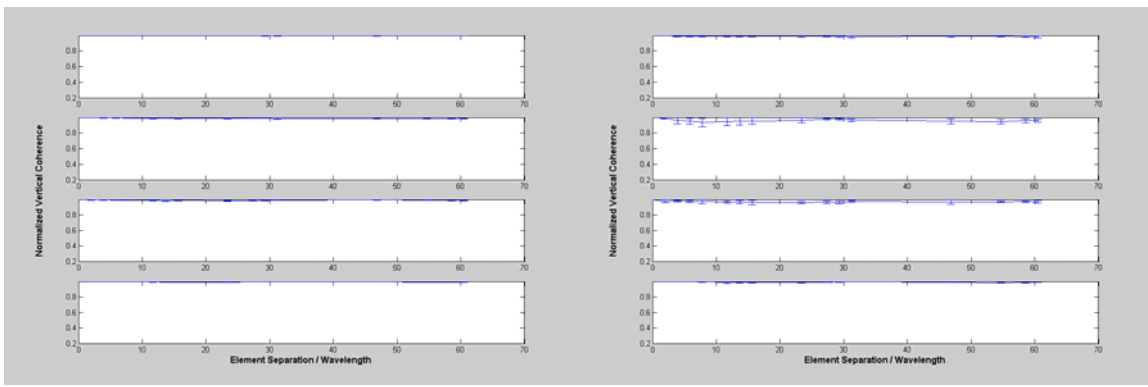
(e)

Figure 17. Effect of Turbulence Strength Parameter at 16 kHz.

(a) Turbulence Strength = Reference, (b) Turbulence Strength = Ref-2, (c) Turbulence Strength = Ref-1, (d) Turbulence Strength = Ref+1, (e) Turbulence Strength = Ref+2

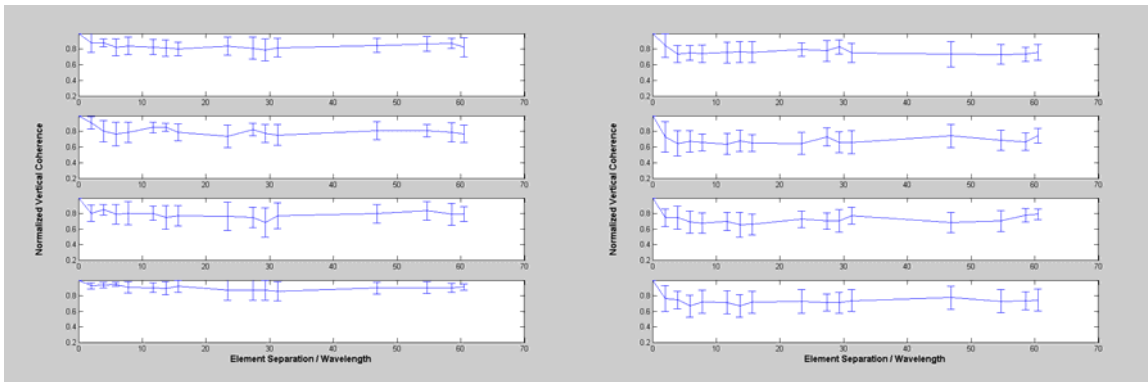


(a)



(b)

(c)



(d)

(e)

Figure 18. Effect of Turbulence Strength Parameter at 20 kHz.

(a) Turbulence Strength = Reference, (b) Turbulence Strength = Ref-2, (c) Turbulence Strength = Ref-1, (d) Turbulence Strength = Ref+1, (e) Turbulence Strength = Ref+2

B. TURBULENCE OUTER LENGTH SCALE

The analysis of the turbulence outer length scale confirmed that acoustic propagation through a turbulent environment is most sensitive to structures on the scale of the Fresnel radius. If the range is constant, the Fresnel radius is a function of frequency only. In this model, the range is kept constant and the frequency range of 4-20 kHz is used. As a result the Fresnel radius values vary from 13.7 m down to 6.1 m. Rather than changing the cutoff scale for each frequency, $k_t = 0.628 \text{ 1/m}$ (outer length scale of $\lambda_t = 10 \text{ m}$) is used as a reference value, consistent with previous work (Duda et al., 1998). Note that this falls within the range of Fresnel scales defined. Thus, the influence of the outer length scale is considered here.

Figures 19 to 22 show the effect of changes in cutoff scale at different frequencies. The vertical correlation is found to exhibit the greatest degradation (most significant scattering) for the largest outer length scale value of 50 m. This result is verified for all frequencies.

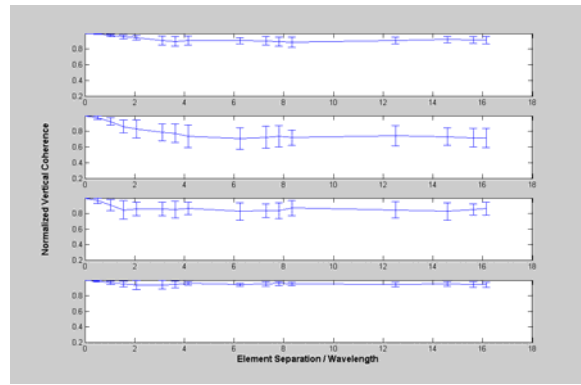
A turbulence outer length scale of 5 m barely produced any visible signal degradation, and a cutoff scale of 2 m produced no observable signal degradation for all frequencies. For these cutoff scale values, the turbulence spectrum does not generate enough perturbation at the Fresnel scale for the frequencies considered. However, as the cutoff scale is increased to 10 m, the part of the spectrum generating perturbations at the Fresnel scale starts to increase, and the signal correlation tends to decrease. This result is then consistent with the expectation of the dominant effect of scattering at the Fresnel scale.

For 4 kHz, the Fresnel scale is 13.7 m. When the reference cutoff scale of 10 m is applied, the perturbations are below the Fresnel scale. Therefore, a cutoff scale value of 25 m has a remarkable effect for this frequency. The same transition may also be observed for 8 kHz, since the Fresnel scale value for this frequency is 9.7 m, which is slightly below the reference cutoff scale. The Fresnel scale values for 16 and 20 kHz are 6.8 and 6.1 m, respectively. When the reference cutoff scale is applied, the perturbations

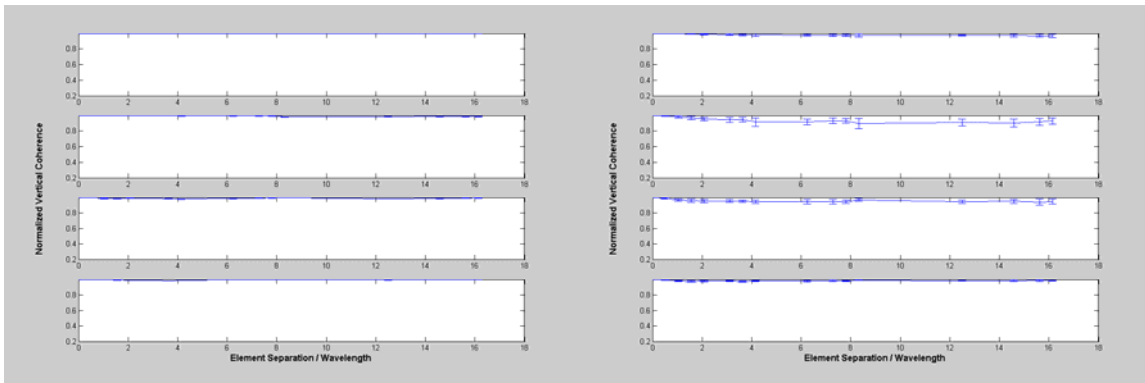
are already beyond the critical threshold. Therefore, increasing the cutoff scale to 25 m for these frequencies does not cause a remarkable degradation in signal coherence.

Comparison of the analysis of 8 kHz versus 16 and 20 kHz verifies that the dissipation of this effect does not occur right beyond the threshold, but several meters beyond the threshold. When a 10 m cut-off scale was applied for 8 kHz, the perturbations are only 0.3 m beyond the threshold. However, these same perturbations are 3.2 and 3.9 m beyond the threshold for 16 and 20 kHz, respectively. The impact of this change of scale on the level of perturbation at the Fresnel scale is readily observed in the spectral plots, displayed previously in Figures 13 and 14. Though an exact value was not calculated, we concluded that if the perturbations are several meters greater than the Fresnel scale, further increase of the cut-off scale doesn't significantly affect the signal coherence. Figures 19 to 22 clearly display the verification of these results.

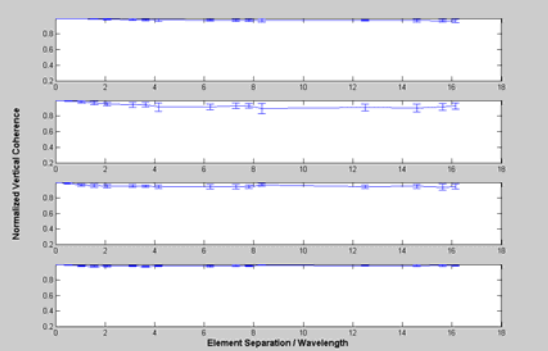
Although larger cutoff scales could have been used for further analysis, the reference value of 10 m was chosen for the remainder of this thesis. The decision was made so that the cutoff scale was consistent with previous research, and because this scale did produce noticeable signal degradation. Therefore, the influence of other parameters could be observed at this cutoff scale.



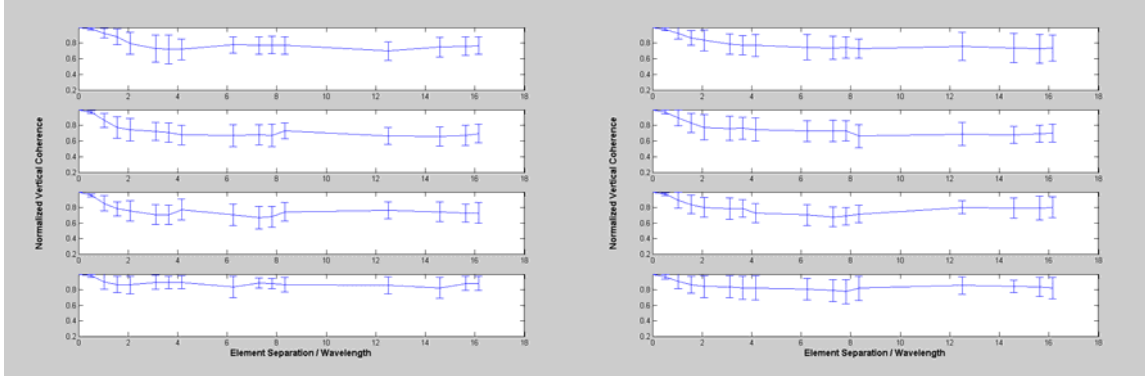
(a)



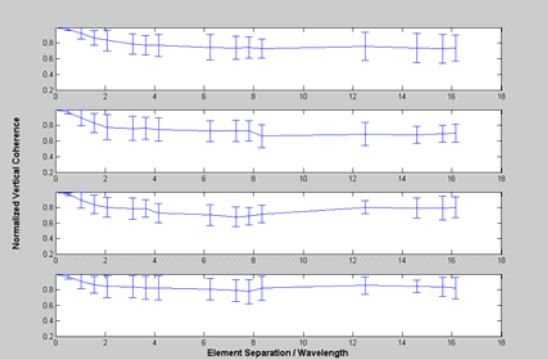
(b)



(c)



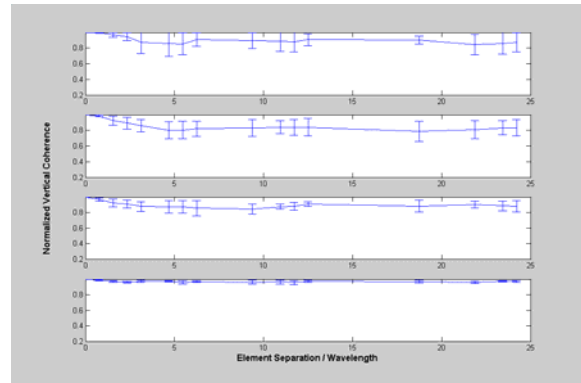
(d)



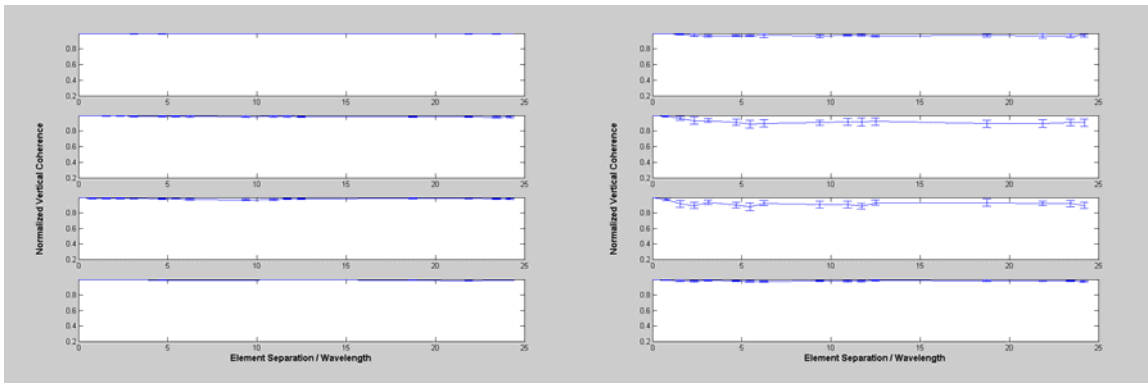
(e)

Figure 19. Effect of Turbulence Outer Length Scale at 4 kHz.

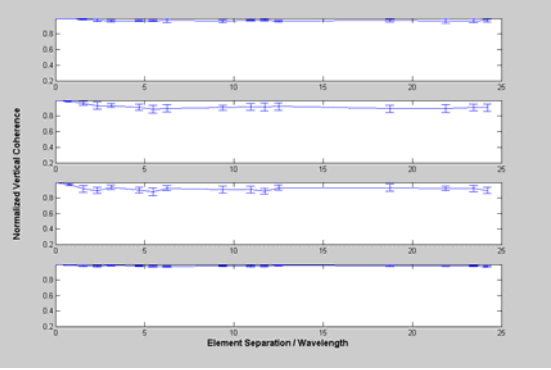
(a) Turbulence Scale = 10 m (Reference Case), (b) Turbulence Scale = 2 m, (c) Turbulence Scale = 5 m, (d) Turbulence Scale = 25 m, (e) Turbulence Scale = 50 m



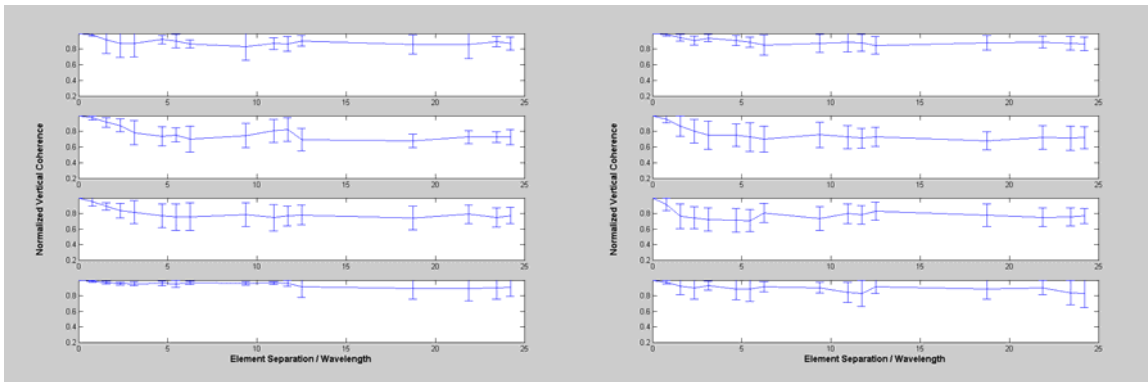
(a)



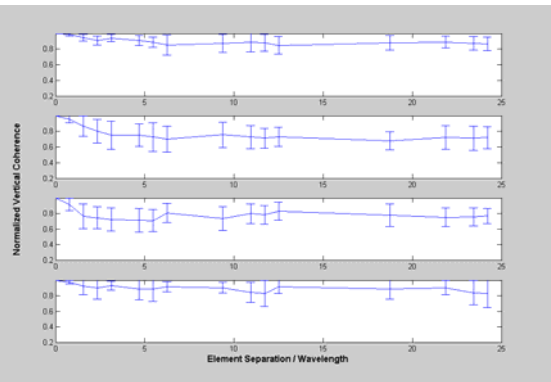
(b)



(c)



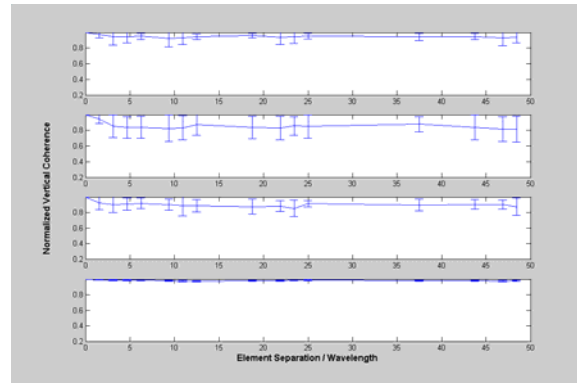
(d)



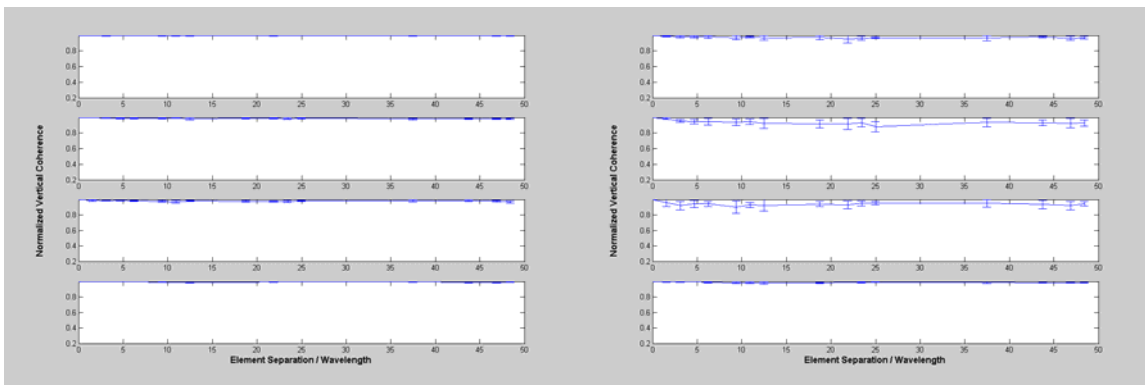
(e)

Figure 20. Effect of Turbulence Outer Length Scale at 8 kHz.

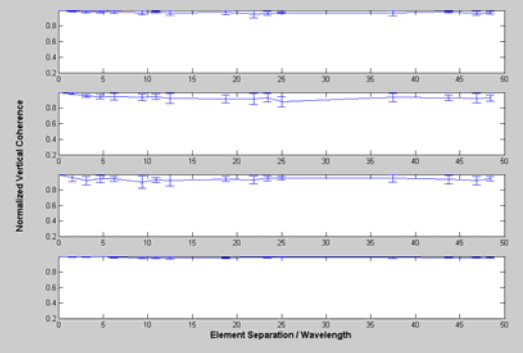
(a) Turbulence Scale = 10 m (Reference Case), (b) Turbulence Scale = 2 m, (c) Turbulence Scale = 5 m, (d) Turbulence Scale = 25 m, (e) Turbulence Scale = 50 m



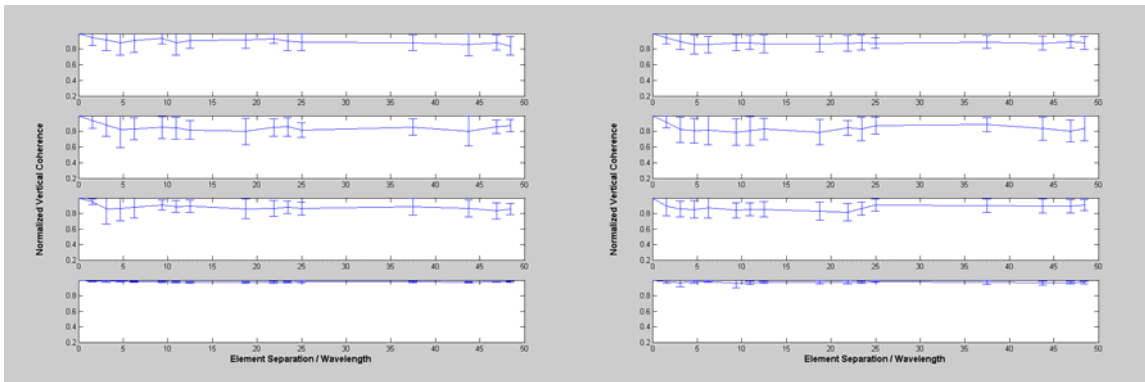
(a)



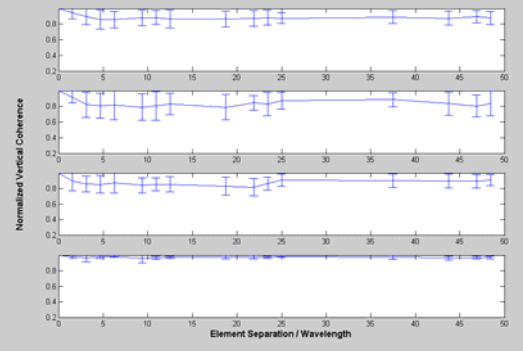
(b)



(c)



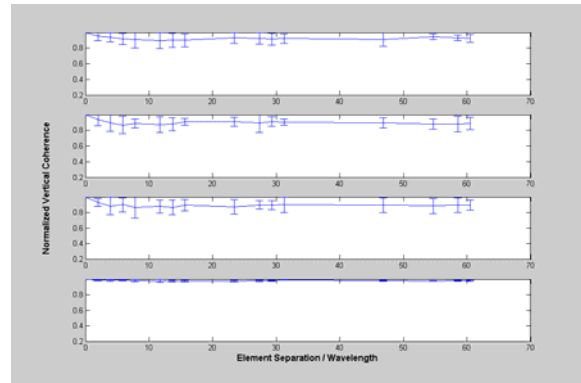
(d)



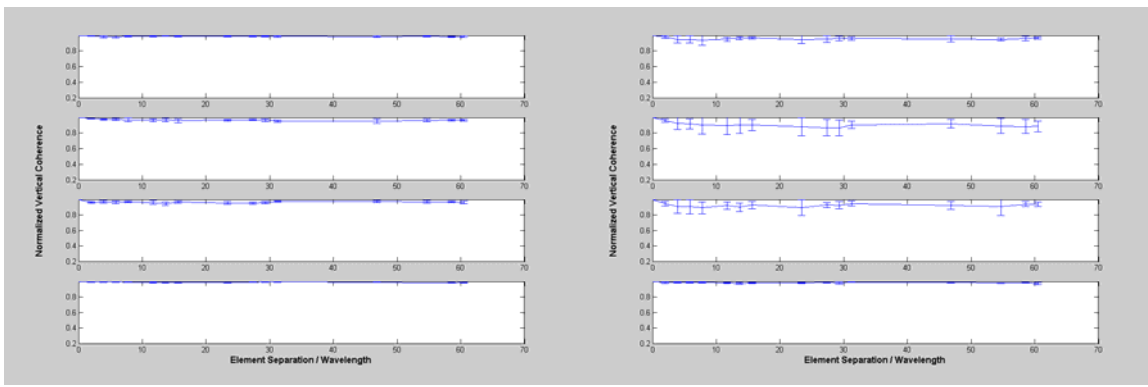
(e)

Figure 21. Effect of Turbulence Outer Length Scale at 16 kHz.

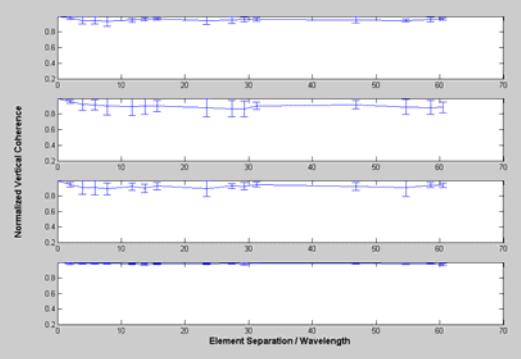
(a) Turbulence Scale = 10 m (Reference Case), (b) Turbulence Scale = 2 m, (c) Turbulence Scale = 5 m, (d) Turbulence Scale = 25 m, (e) Turbulence Scale = 50 m



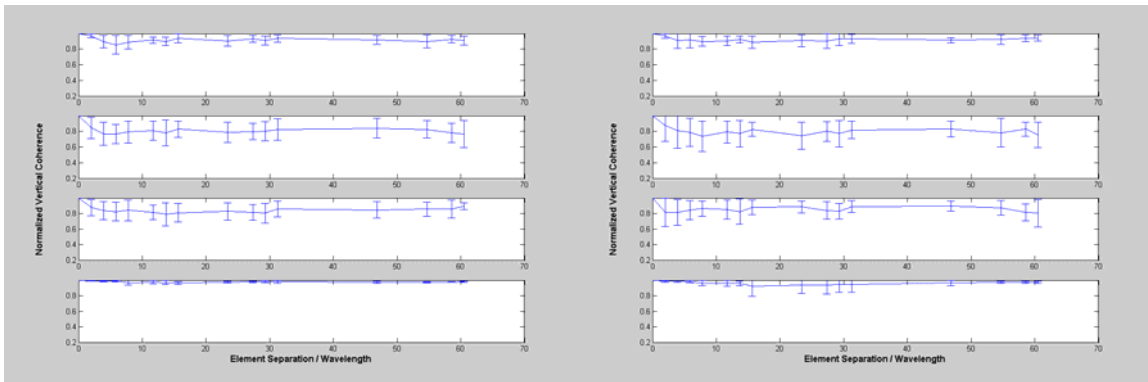
(a)



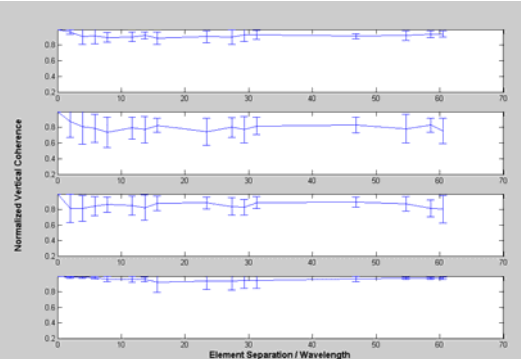
(b)



(c)



(d)



(e)

Figure 22. Effect of Turbulence Outer Length Scale at 20 kHz.

(a) Turbulence Scale = 10 m (Reference Case), (b) Turbulence Scale = 2 m, (c) Turbulence Scale = 5 m, (d) Turbulence Scale = 25 m, (e) Turbulence Scale = 50 m

C. CURVATURE ANALYSIS

Previous work by Duda and Bowlin (1994) examined the stability of long-range acoustic ray propagation through internal wave fluctuations in deep water. They found that the stability of the rays propagating through various depths of the waveguide were related to mean values of $\log|U|$, where

$$U = c \left(\frac{\partial^2 c}{\partial z^2} \right) \left/ \left(\frac{\partial c}{\partial z} \right)^2 \right., \quad (93)$$

and $c = c(z)$ is the depth-dependent sound speed profile. More recent work by Brown, et al. (2004, in press) also showed theoretically how long-range ray stability may be dominated by features of the background sound speed profile.

While both of the aforementioned analyses were concerned with long-range, deep water propagation, the analysis presented here suggests a potentially similar influence of the background sound speed profile. Therefore, we shall now examine a similar measure of the direct path propagation in the shallow water environment presented here. Specifically, the depth-dependent parameter U , defined above, will be computed for the four profiles examined. A simple ray-trace model will then be employed to compute ray trajectories through the unperturbed (no turbulence) background profiles and the subsequent average of $\log|U|$ along the ray path will be determined. While Duda and Bowlin (1994) included their internal wave perturbations in the calculations of U , the turbulence fluctuations are not expected to significantly affect the average of $\log|U|$ along the direct-path ray trajectories.

In order to compute U , the discretely sampled sound speed profiles provided by the measured data sets must be fitted by some twice differentiable function. Cubic splines are employed here. Although Duda and Bowlin (1994) refer to possible spurious values from such cubic polynomials, this tends to be a more significant problem when the spacing between measured sound speed values is not uniform in depth. In the case of the

ASIAEX data sets used here, the depth sampling is uniform, so the use of cubic polynomials is expected to be more stable.

As an example of the data fit achieved by the cubic spline technique, Figure 23 displays the CTM profile data (as discrete points) compared to data interpolated from the cubic polynomial. This comparison shows the density of measured data points relative to the observed curvature in the profile, and justifies the use of the cubic splines to fit the data. A direct calculation of $\log|U|$ is then possible. Figure 24 provides the results of these calculations for all four sound speed profiles considered.

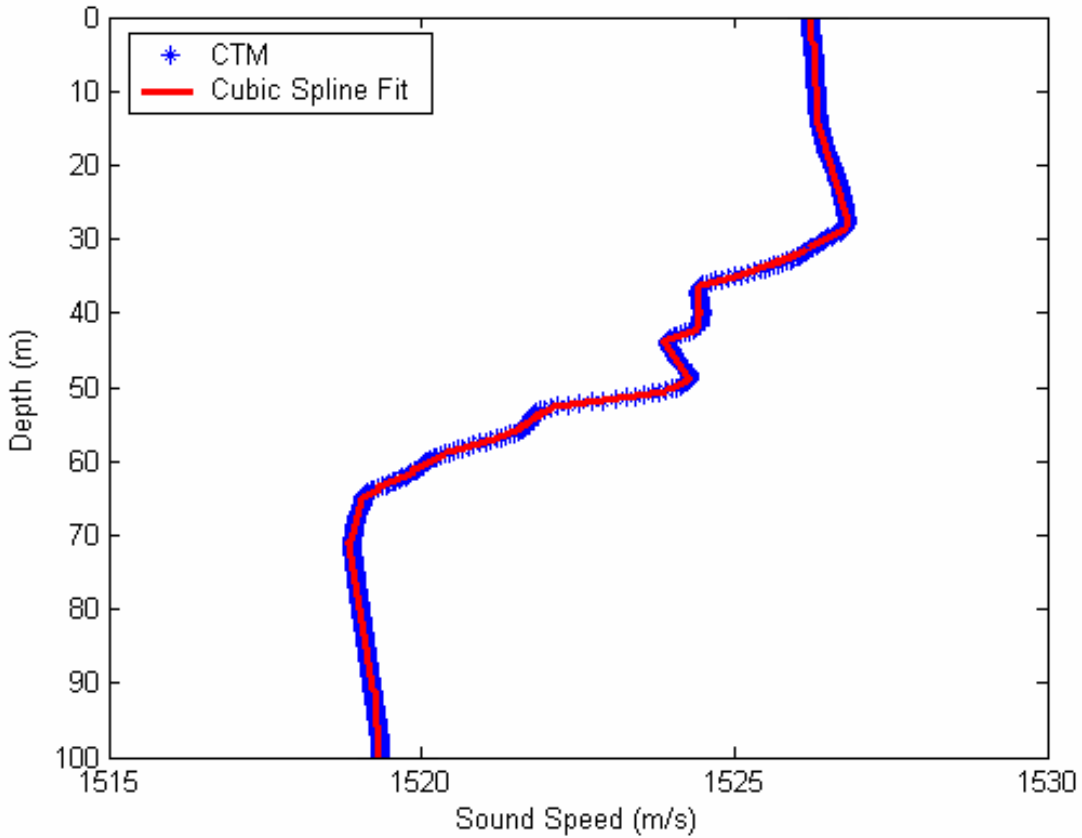


Figure 23. Measured Sound speed Data Compared to Cubic Spline Fit for CTM Profile.

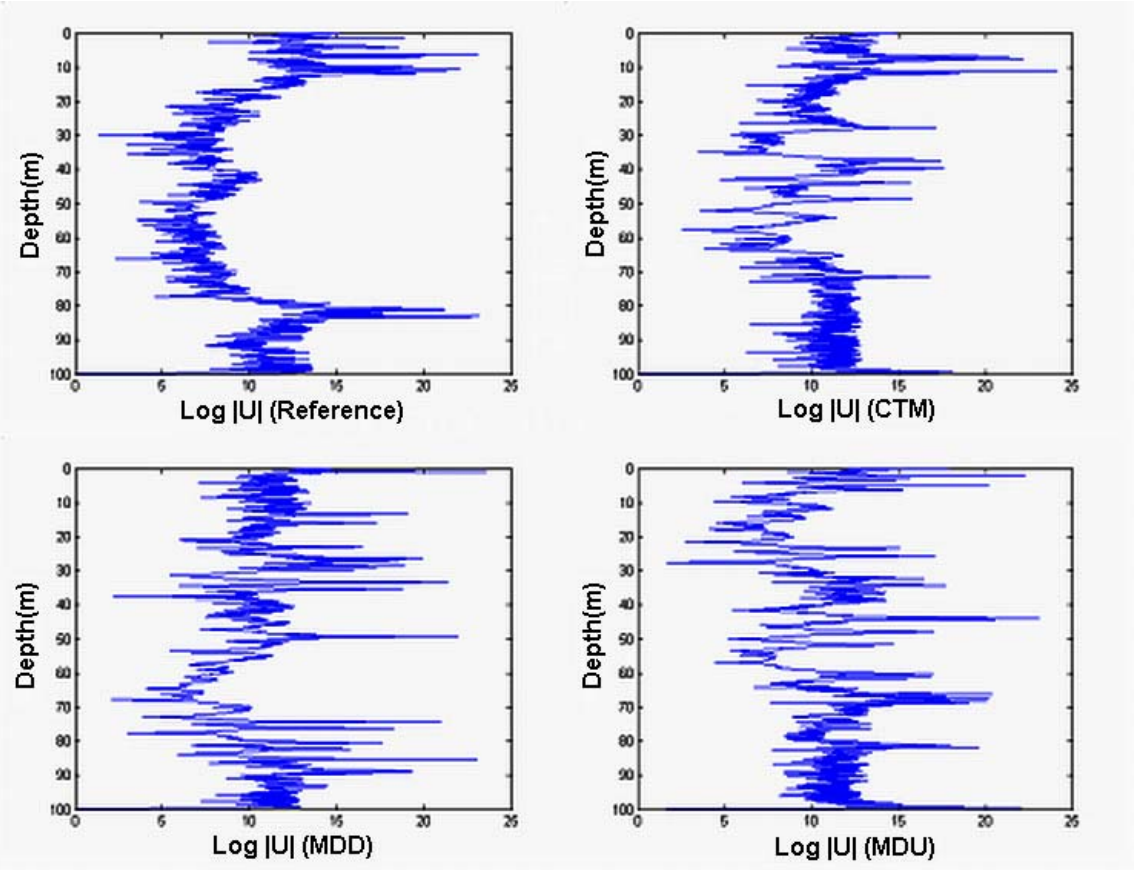


Figure 24. Profiles of $\log|U|$ for the four environmental profiles examined: reference (upper left); CTM (upper right); MDD (lower left); MDU (lower right).

To compute ray trajectories, a simple 4th-order Runge-Kutta algorithm was employed. Such an algorithm requires a continuous sampling of both the sound speed profile and its first derivative, both of which are provided by the cubic spline interpolation. Although the code can accurately handle smooth boundary reflections, such ray paths were not of interest here, so only those rays without boundary reflections were saved for analysis.

At each range step along each ray path, the value of $\log|U|$ was then evaluated. By simply summing all such values and dividing by the number of range steps in the calculation out to 500m, an along-ray average of $\log|U|$ was computed. In Figure (4),

sample plots of ray paths in the reference environment for three different source depths (30m, 50m, and 70m) are displayed. It is important to note that, in order to compute a well-sampled profile of the along-ray mean of $\log|U|$, a dense sampling of ray arrival depths at the final range (500m) is needed. Because the structure of the background sound speed profiles tended to cause a divergence of ray paths near the center of the water column (refer to 50m source depth ray paths in Figure 25), various techniques were used to increase the density of ray launch angles near 0° , and the minimum and maximum values of launch angles were varied to insure arrival depths between the depths of interest (about 20m–80m). Results of this analysis are also displayed in Figure 25 for the same environment and source depths, but using an altered code that increases the density of ray paths for adequate sampling of the final profile of the along-ray mean of $\log|U|$.

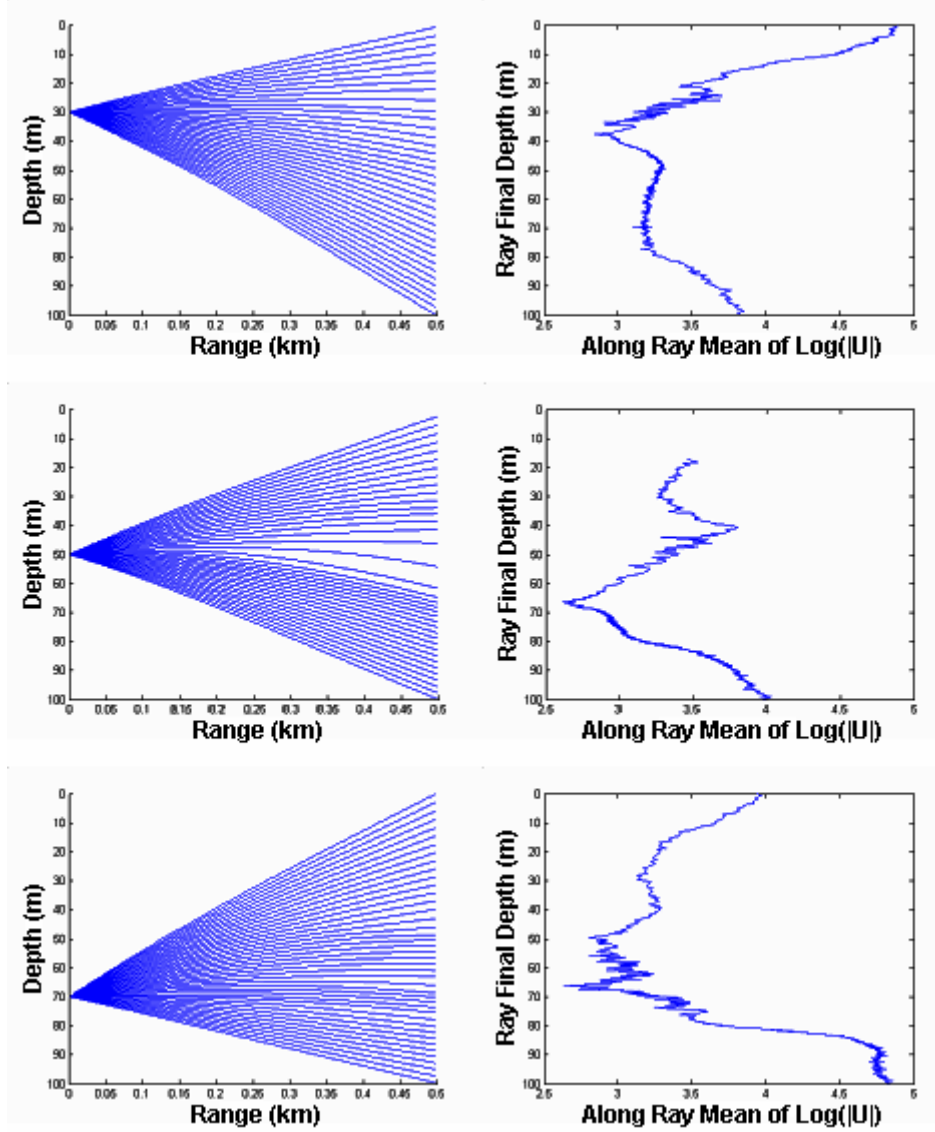


Figure 25. Sample ray paths for the reference environment and the corresponding profiles of the along-ray mean of $\log|U|$ for three source depths: 30m (upper plots); 50m (middle plots); 70m (lower plots).

The profiles of the along-ray mean of $\log|U|$ were computed for all background sound speed profile environments and source depths considered. Once these profiles were determined, a final average value over the depth of the sub-arrays was then computed. These unique values are tabulated and presented in the following sections to

compare with the observed dependence of signal correlation on propagation paths through the various environments.

D. SOURCE DEPTH

The depth of the source will have a direct influence on the propagation paths between the source and receiver elements as dictated by the sound speed profile. The reference SSP is used for the analysis of source depth influence. The reference SSP is approximately isospeed over the depth intervals 0-20 m and 80-100 m, and as a consequence doesn't exhibit a remarkable variability at these depths. There is a thermocline between the depths 20-80 m, and so propagation through this region undergoes significant refraction.

As the source depth was increased from 30 to 40 and then 50 m, an observable pattern existed in the change of signal coherence for all frequencies. When the source was placed at 30 m, the signal mostly propagated in the upper, isospeed part of the waveguide. These paths appear coincident with little signal degradation. As the depth of the source is lowered to 40 m, the signal partly propagates through the thermocline. This caused a slight decrease in the correlation for all depths and frequencies. When the source depth was changed to 50 m, the sub-arrays at 45 and 55 m received signals which traversed along the thermocline. The signals recorded at these sub-arrays exhibit a remarkable drop in the signal coherence. Verification of these results is shown in Figures 26 to 29 (parts a, b and c of figures).

When the source was lowered to 60 m, signals at the upper sub-arrays, 35 and 45 m, observed significantly more variability compared to the lower sub-arrays, consistent with higher variability along those paths propagating through regions of higher sound speed gradient. Placing the source at a depth of 70 m didn't cause a noteworthy degradation of correlation at any receiver depths for all frequencies tested in this research.

Due to this apparent correlation between background sound speed gradient, propagation paths, and signal coherence, the analysis of the variable source depth effect

includes the effect of SSP curvature, as described in the previous section. The effect of SSP curvature was not consistent for all results of source depths. However, considering that this effect was originally derived for deep and long-range propagation, the exceptions may be due to the shallow water, short-range nature of the problem.

The sub-array averages of correlation values are calculated to provide a comparison between the signal coherence and SSP curvature. All of the correlation curves generally exhibited a decrease in coherence over the first few wavelengths, and a slightly increasing coherence pattern near the last wavelength. The stabilized region of the correlation curve is extracted after removing the correlation values corresponding to the first five and the last wavelengths. These stabilized correlation curve values were then used to generate an average coherence value for each sub-array.

When there was a noticeable relative difference between the correlation values of receivers, the relative change of the SSP curvature parameter was consistent. For the source depths of 30 and 40 m, a significant decorrelation was not noted at any depths and frequencies. Therefore, the influence of SSP curvature isn't analyzed for these source depths. The sub-array averages of along-ray means of $\log|U|$ for the reference sound speed profile and depths of 50, 60, and 70 m are exhibited in Table 5. The sub-array averages of correlation values for source depths of 50, 60, 70 m are exhibited in Tables 6 to 8.

Source Receiver	50 m	60 m	70 m
35-40 m	3.54	3.33	3.26
45-50 m	3.43	3.13	2.97
55-60 m	3.06	2.82	3.00
65-70 m	2.76	3.00	3.03

Table 5. Sub-Array Averages of Along-Ray Means of $\log|U|$.

Frequency Receiver	4 kHz	8 kHz	16 kHz	20 kHz
35-40 m	0.91	0.88	0.94	0.92
45-50 m	0.75	0.82	0.85	0.89
55-60 m	0.85	0.88	0.89	0.88
65-70 m	0.95	0.97	0.98	0.98

Table 6. Sub-Array Averages of Correlation Values for Source Depth = 50 meters.

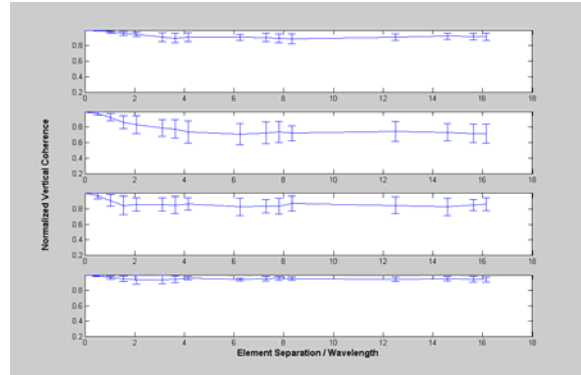
Frequency Receiver	4 kHz	8 kHz	16 kHz	20 kHz
35-40 m	0.86	0.86	0.90	0.85
45-50 m	0.78	0.76	0.84	0.89
55-60 m	0.94	0.94	0.97	0.93
65-70 m	0.94	0.95	0.97	0.97

Table 7. Sub-Array Averages of Correlation Values for Source Depth = 60 meters.

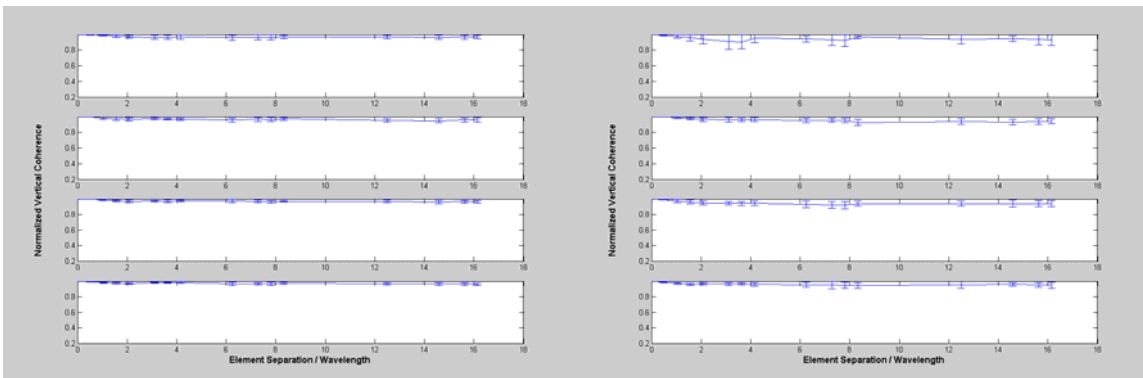
Frequency Receiver	4 kHz	8 kHz	16 kHz	20 kHz
35-40 m	0.84	0.89	0.92	0.87
45-50 m	0.87	0.89	0.89	0.93
55-60 m	0.92	0.86	0.93	0.89
65-70 m	0.95	0.93	0.93	0.93

Table 8. Sub-Array Averages of Correlation Values for Source Depth = 70 meters.

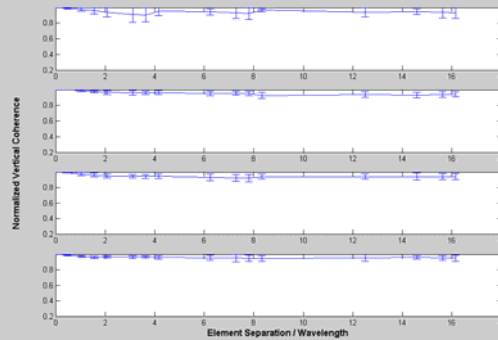
As the average along-ray mean values of $\log|U|$ corresponding to each sub-array increase, the signal coherence is expected to decrease. This negative effect of SSP curvature may be observed by cross-examining Tables 5 to 8. There are exceptions of this effect, which again may be due in part to the shallow water, short-range nature of the problem.



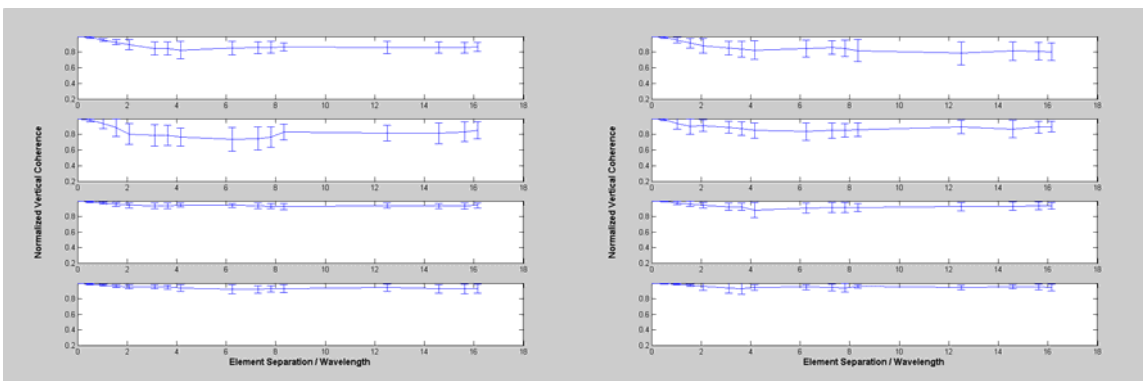
(a)



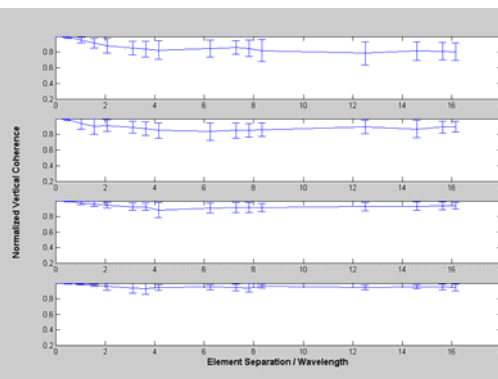
(b)



(c)



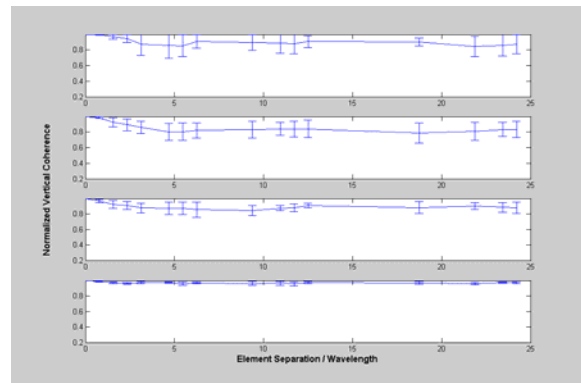
(d)



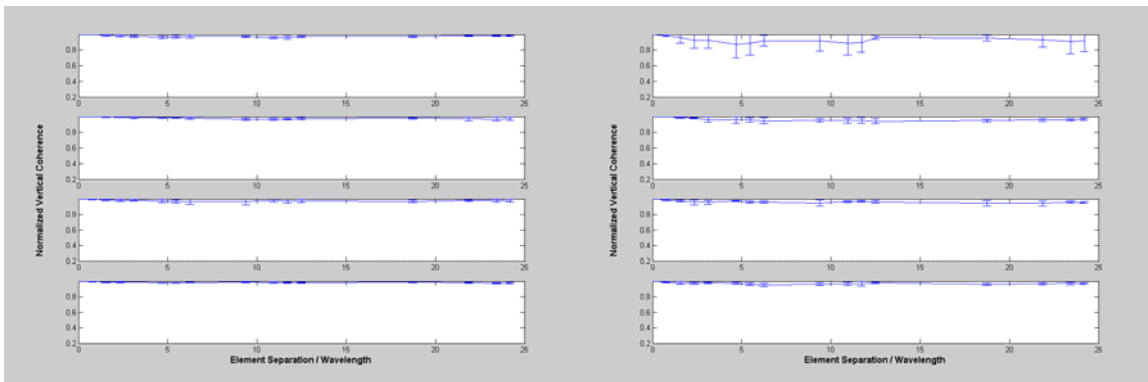
(e)

Figure 26. Effect of Source Depth Variation at 4 kHz.

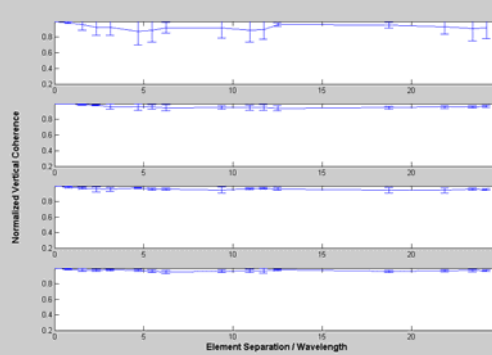
(a) Source Depth = 50 m (Reference Case), (b) Source Depth = 30 m, (c) Source Depth = 40 m, (d) Source Depth = 60 m, (e) Source Depth = 70 m



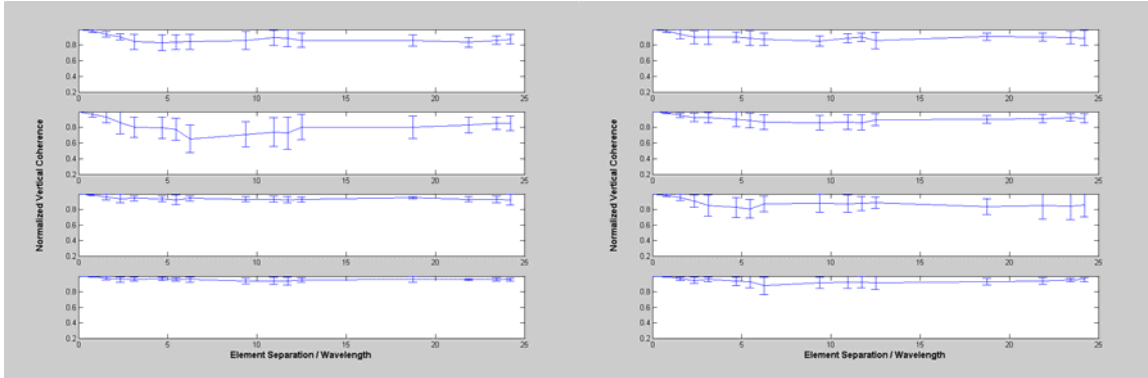
(a)



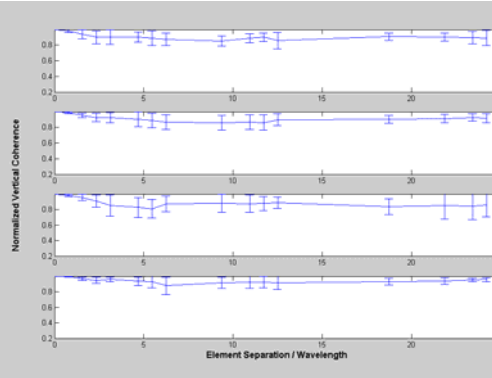
(b)



(c)



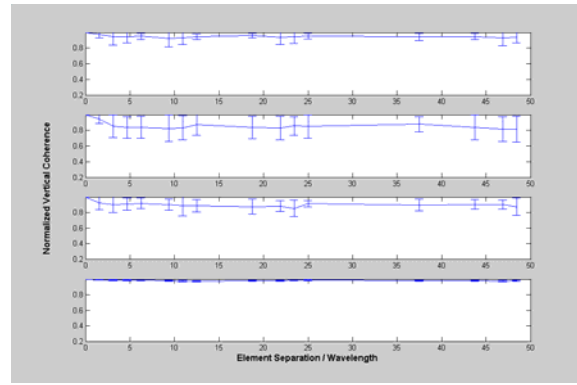
(d)



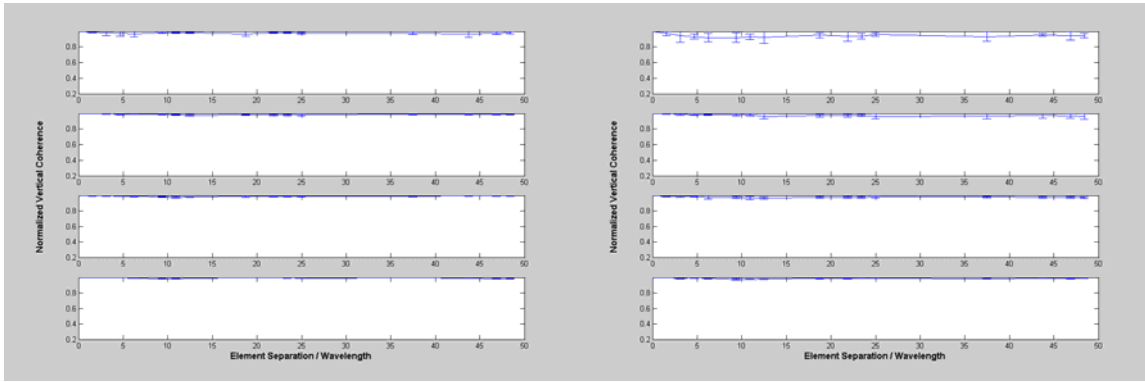
(e)

Figure 27. Effect of Source Depth Variation at 8 kHz.

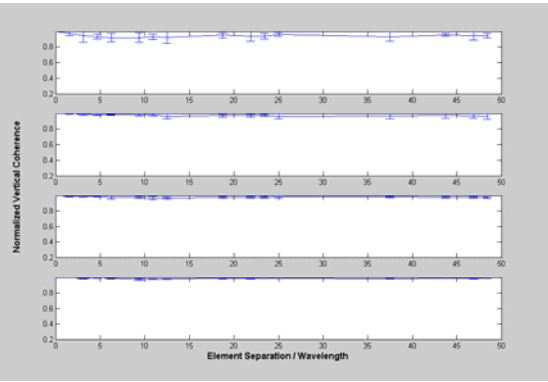
(a) Source Depth = 50 m (Reference Case), (b) Source Depth = 30 m, (c) Source Depth = 40 m, (d) Source Depth = 60 m, (e) Source Depth = 70 m



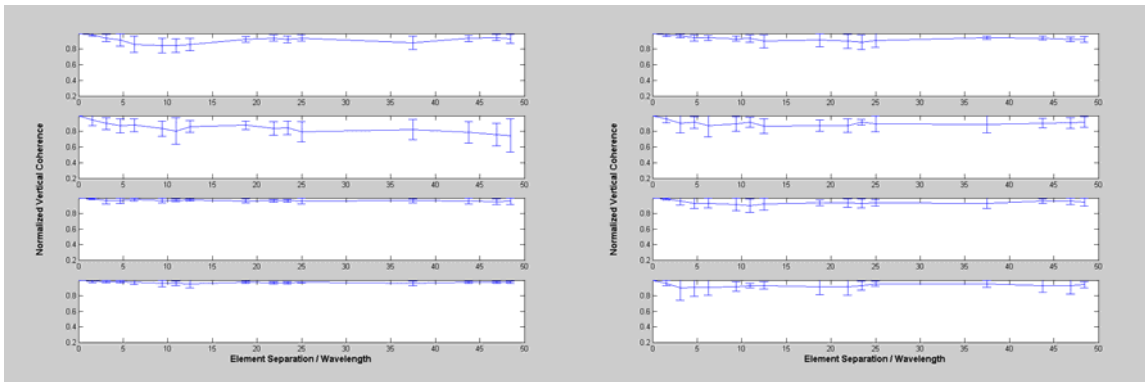
(a)



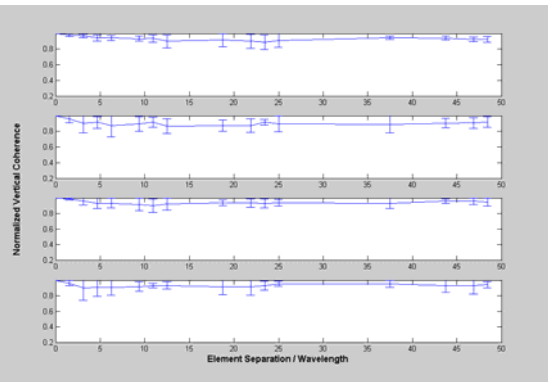
(b)



(c)



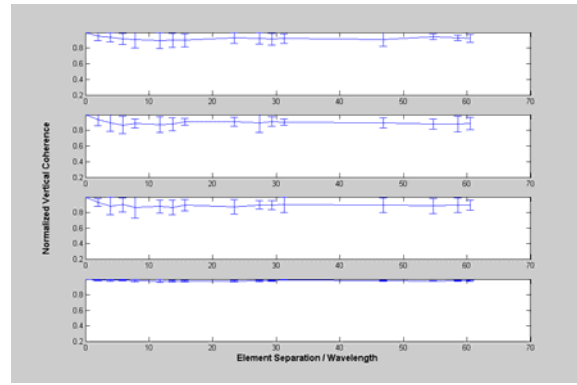
(d)



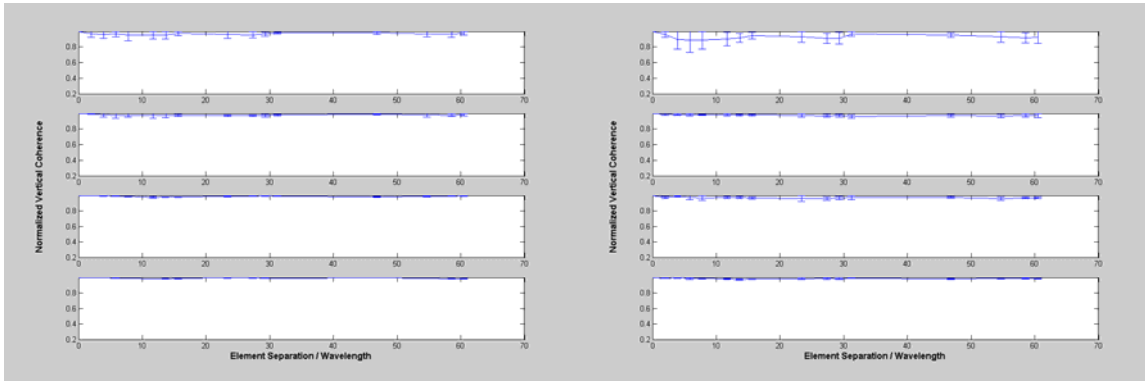
(e)

Figure 28. Effect of Source Depth Variation at 16 kHz.

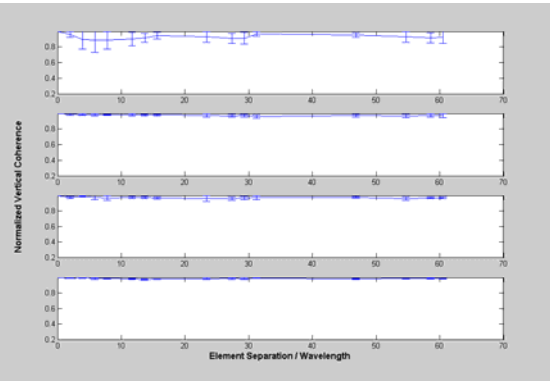
(a) Source Depth = 50 m (Reference Case), (b) Source Depth = 30 m, (c) Source Depth = 40 m, (d) Source Depth = 60 m, (e) Source Depth = 70 m



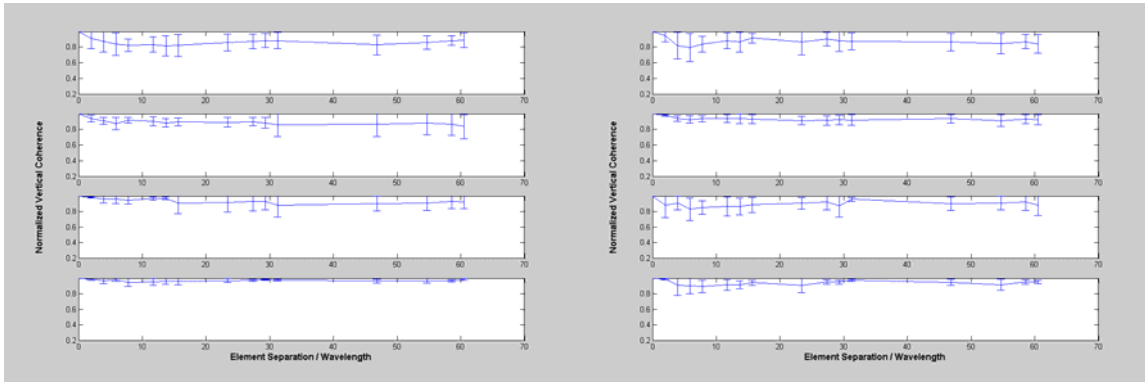
(a)



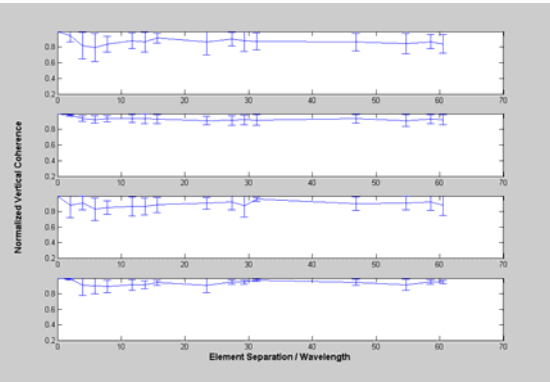
(b)



(c)



(d)



(e)

Figure 29. Effect of Source Depth Variation at 20 kHz.

(a) Source Depth = 50 m (Reference Case), (b) Source Depth = 30 m, (c) Source Depth = 40 m, (d) Source Depth = 60 m, (e) Source Depth = 70 m

E. SOUND-SPEED PROFILE

Four different background sound speed profiles were examined in this research. Details of these profiles were described in Chapter III. During the following analysis of the effect of background SSP, the source depth was fixed at 50 m.

As noted previously, the reference SSP is nearly isospeed in the intervals 0-20 m and 80-100 m, and contains a thermocline between the depths 20-80 m. The signal coherence was already observed to suffer the most degradation when the signal propagates through the thermocline. Sub-arrays located at 45-50 and 55-60 m were found to receive the most degraded signals when the reference SSP is used. This observation is verified for all frequencies and the results are exhibited in Figures 30 to 33 (upper left parts of all figures).

The CTM sound speed profile has depth properties similar to the reference SSP. However, the CTM profile has more variability in the thermocline region. This increase of variability in sound speed is found to produce even more degradation in signal coherence. A decrease in correlation at all depths is observed. It must be noted that the signals on the sub-arrays located at 45-50 and 55-60 m still exhibit the greatest degradation compared to other sub-arrays, presumably since they are located in the middle of thermocline region. These results may be confirmed by looking at Figures 30 to 33 (upper right parts of all figures).

The MDD sound speed profile is mostly isospeed over the depths 0-65 m (with the exception of a single “jump” around 30 m). Therefore, based on the previous findings, we may expect that signals from a 50 m source will not be as severely degraded as they are with the reference profile, since most of the propagation occurs in this upper, isospeed portion of the profile. The analysis of the results using the MDD sound speed profile consistently verified this assumption and the results are displayed in Figures 30 to 33 (lower left parts of all figures).

The MDU sound speed profile has effectively no upper isospeed region. The thermocline exists from around 5 m down to around 65 m, below which the profile is nearly isospeed. The overall variability of the MDU sound speed profile appears less than

the CTM sound speed profile. Therefore, it may be anticipated that the results of these two sound speed profiles from a 50 m source would be similar, with the MDU profile having a weaker effect on signal coherence. The model verified these assumptions and the results are shown in Figures 30 to 33 (upper right parts of all figures).

Similar to analysis of source depth, effect of SSP curvature is also analyzed for changes in the background sound speed profile. The most consistent results were noted for the reference SSP and the CTM sound speed profile. The sub-array averages of along-ray means of $\log|U|$ for the 50 m source depth in the various sound speed profiles are tabulated in Table 9. The sub-array averages of correlation values for the various sound speed profiles are displayed in Tables 10-11.

SSP Receiver	Reference	CTM	MDD	MDU
35-40 m	3.54	4.60	4.67	4.62
45-50 m	3.43	4.86	5.30	4.27
55-60 m	3.06	4.05	4.38	4.26
65-70 m	2.76	3.69	3.87	4.26

Table 9. Sub-array averages of along-ray means of $\log|U|$ for the source at 50 m depth.

Frequency Receiver	4 kHz	8 kHz	16 kHz	20 kHz
35-40 m	0.91	0.88	0.94	0.91
45-50 m	0.75	0.82	0.85	0.75
55-60 m	0.85	0.88	0.89	0.85
65-70 m	0.95	0.97	0.98	0.95

Table 10. Sub-Array Averages of Correlation Values for the reference SSP.

Frequency Receiver \	4 kHz	8 kHz	16 kHz	20 kHz
35-40 m	0.94	0.94	0.94	0.88
45-50 m	0.72	0.71	0.73	0.78
55-60 m	0.67	0.65	0.74	0.74
65-70 m	0.79	0.85	0.88	0.90

Table 11. Sub-Array Averages of Correlation Values for the CTM sound speed profile.

As the average along-ray mean values of $\log|U|$ corresponding to each sub-array increase, the signal coherence may be expected to decrease. The results of the analysis presented here verify this expectation with some exceptions. The results may be best understood by cross-examining Tables 9 to 11. The exceptions are possibly due to the short-range nature of the propagation examined in this work.

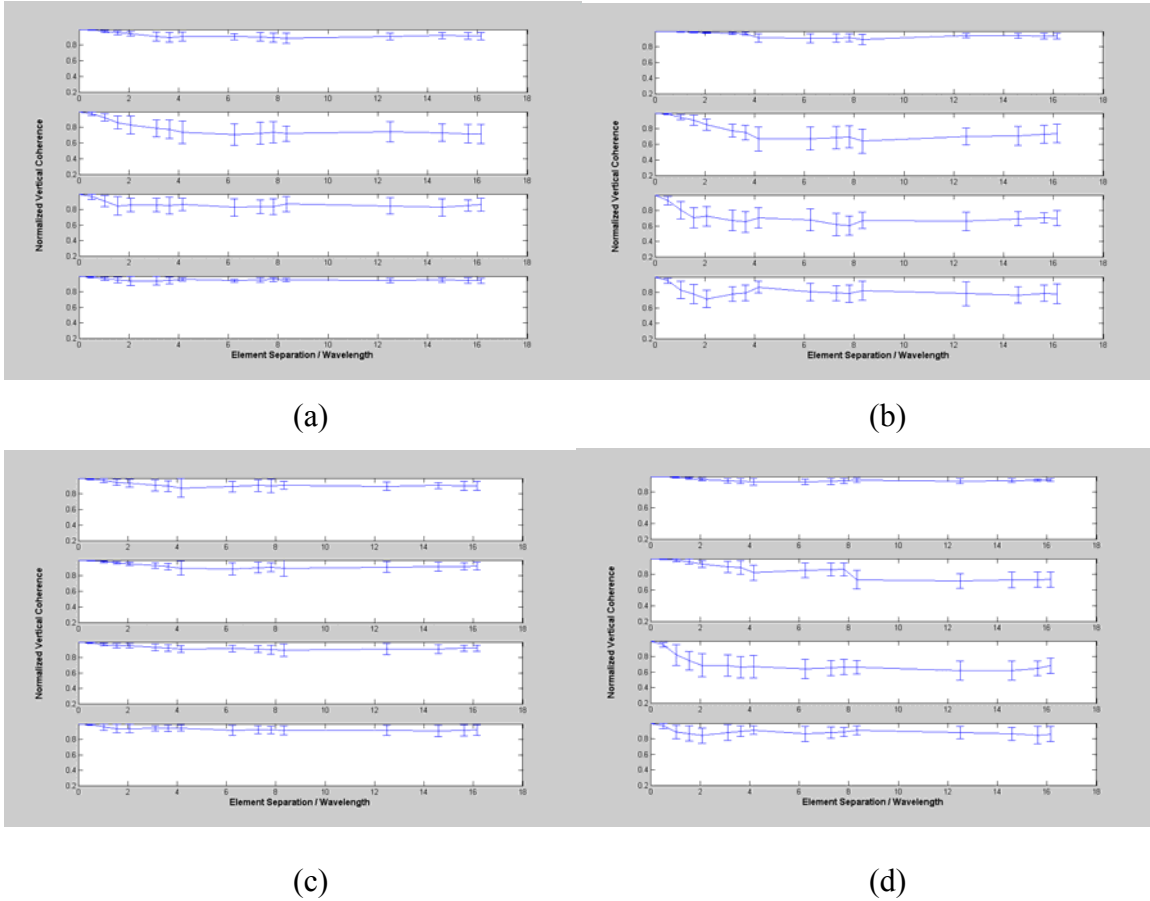


Figure 30. Effect of Background Sound-Speed Profile at 4 kHz.
 (a) SSP = Reference Case, (b) SSP = CTM, (c) SSP = MDD, (d) SSP = MDU

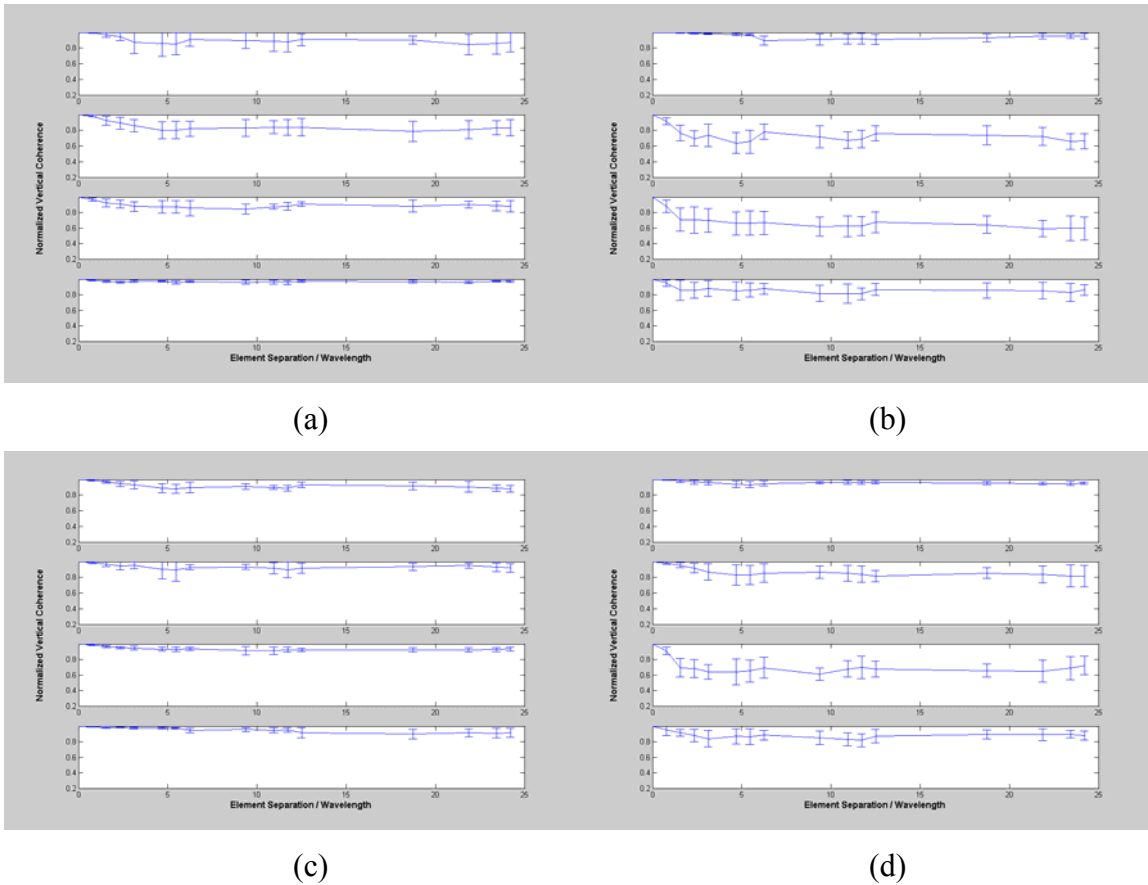


Figure 31. Effect of Background Sound-Speed Profile at 8 kHz.
 (a) SSP = Reference Case, (b) SSP = CTM, (c) SSP = MDD, (d) SSP = MDU

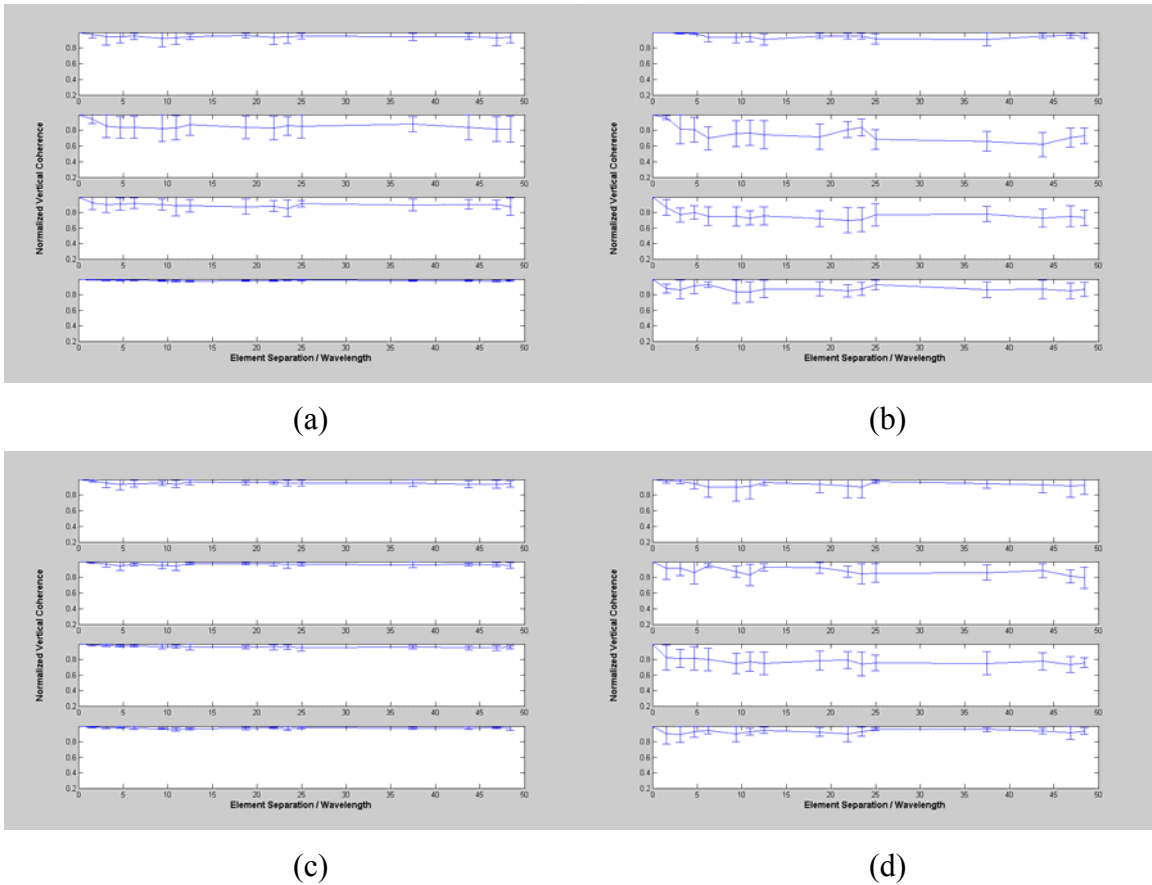


Figure 32. Effect of Background Sound-Speed Profile at 16 kHz.

(a) SSP = Reference Case, (b) SSP = CTM, (c) SSP = MDD, (d) SSP = MDU

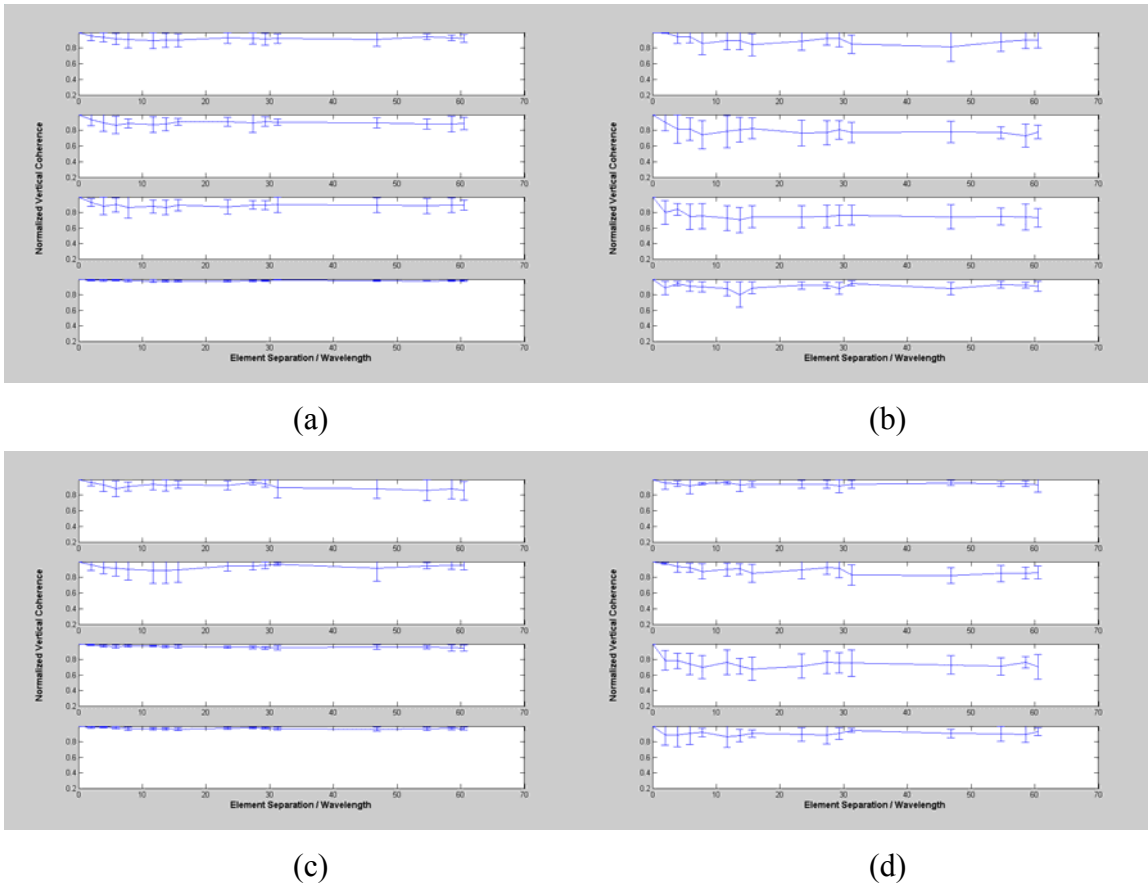


Figure 33. Effect of Background Sound-Speed Profile at 20 kHz.
 (a) SSP = Reference Case, (b) SSP = CTM, (c) SSP = MDD, (d) SSP = MDU

THIS PAGE INTENTIONALLY LEFT BLANK

V. SUMMARY

A. CONCLUSIONS

The motivation of this research was to develop a better understanding of the influence of turbulence and environmental variability on broadband acoustic coherence. The MMPE model was used to simulate the effects of a turbulent environment on such broadband acoustic propagation. Realistic turbulence perturbations based on well established statistical models were incorporated into the MMPE model, making investigations of such effects on signal coherence easily accessible for a variety of environmental factors and source/receiver geometries. The background sound speed profiles and the model geometry were similar to a component of one of the East China Sea experiments conducted during ASIAEX. Effects of turbulence strength, turbulence cut-off scale, background sound speed profile, frequency and source/receiver geometries on short range, direct-path propagation were examined.

Vertical correlation was used to quantify the coherence of the received signal at four vertical sub-arrays located at a fixed range from the source. Each case was simulated 10 times to simple statistics (mean and standard deviation) of the signal decorrelation due to turbulence.

It was observed that the turbulence strength, a parameter that directly affects the RMS magnitude of the turbulence perturbation, exhibited a positive correlation with signal degradation for all frequencies up to 20 kHz, as expected. Essentially, this simply states that the stronger the sound speed perturbations are, the stronger the acoustic signal degradation will be.

The analysis of the turbulence outer length scale also confirmed the expected result that acoustic propagation through a turbulent environment is most sensitive to structures on the scale of the Fresnel radius. When the perturbations are already greater than the Fresnel scale, further increase in cut-off scale (even with increases in total RMS

perturbation strength) didn't affect the signal coherence. An exact value was not calculated for the critical excess value beyond which the coherence is not affected remarkably. However, it was observed that if the turbulence cut-off scale is several meters greater than the Fresnel scale, then further increases of the cut-off scale do not produce a noteworthy effect on the signal coherence.

Source-receiver depth and background SSP were found, somewhat surprisingly, to have a significant influence on the signal coherence. This was not expected because there was no direct relationship between the background profile and the structure of the turbulence, and because the propagation distances were so short that such influences were not expected to have enough time to "build up" along the path. It was confirmed that propagation through a thermocline has greater (negative) effect on signal coherence than the isospeed regions of the SSP. Thus, the signal stability appears to be strongly dependent upon the propagation path through the background profile (without turbulence).

Due to these observations, an attempt was made to compare these results with similar findings of signal stability dependence in deep ocean, long-range propagation on sound speed profile curvature. The analysis of the SSP curvature performed here was partly consistent with the findings of the signal coherence. Most notably, when there were significant relative differences between the correlation values of the sub-arrays, the relative differences of the mean curvature parameter along the ray paths were consistent.

B. RECOMMENDATIONS AND FUTURE WORK

The findings of the significance of the structure of the background sound speed profile were rather surprising, but of considerable significance. Such findings could result in changes in the operation of various underwater acoustic systems. For example, tactical systems (e.g., mine-hunting UUVs) may be able to improve their detection capabilities by determining their optimal operating depths based on in situ measurements of the

background profile. Depth variable acoustic communication systems may also be able to optimize their performance in a similar fashion.

While the analysis of SSP curvature performed in this thesis showed some consistency with the signal coherence results, it is important to recall that this measure was originally derived for deep and long-range propagation. It is possible, therefore, that another measure of the interaction of the propagation paths with the background profile may be better suited for prediction of signal degradation. Future work may then examine other such measures.

It should also be noted that this analysis assumed a uniform turbulence perturbation field. The effects of depth or range variability of the turbulence is unknown, as is any obvious correlation with depth or range variability of the background profile. More sophisticated oceanographic models of turbulence would be needed to generate the necessary realizations of turbulent fluctuations in order to study these effects.

Finally, although this modeling effort was based on the experimental geometry employed during the ASIAEX studies in the East China Sea, the measured data sets did not include any direct measurements of turbulence structures. It would be of great benefit in a future experiment to simultaneously measure both signal coherence and water column fine-scale structure. The validity of this numerical approach may then be confirmed, and further numerical studies could then be performed with confidence. Our understanding of the impact of small-scale ocean fluctuations on various acoustic systems' performance could then be enhanced, and future system designs could be improved.

THIS PAGE INTENTIONALLY LEFT BLANK

LIST OF REFERENCES

- 1) Smith, K.B. "Convergence, Stability, and Variability of Shallow Water Acoustic Predictions Using a Split-step Fourier Parabolic Equation Model," *J. Comp. Acoust.*, Volume 9, Number 1, September 1999
- 2) Tappert, F. D. "The Parabolic Approximation Method," in *Lecture Notes in Physics*, Vol. 70, Wave Propagation and Underwater Acoustics, edited by J. B. Keller and J. S. Papadakis (Springer-Verlag, New York, 1977)
- 3) Dahl, P. H. "ASIAEX, East China Sea, Cruise Report of the Activities of the R/V Melville 29 May to 9 June 2001," Applied Physics Laboratory, University of Washington, Seattle, WA, July 2001
- 4) Hardin, R. H. and Tappert, F. D. "Applications of the Split-step Fourier Method to the Numerical Solution of Nonlinear and Variable Coefficient Wave Equations," *SIAM Rev.* 15, 1973
- 5) Thomson, D.J. and Chapman, N.R. "A wide-angle split step algorithm for the parabolic equation," *J. Acoust. Soc. Am.* 74, 1848 (1983)
- 6) Tatarskii, V.I. "Wave propagation in a Turbulent Medium," McGraw-Hill, New York, 1961
- 7) Duda, T.F., Flatte, S.M., Creamer, D.B. "Modeling Meter-Scale Acoustic Intensity Fluctuations From Oceanic Fine Structure and Microstructure," *Journal of Geophysical Research*, Vol. 93, No. C5, Pages 5130-5142, May 15, 1988
- 8) Henyey, F.S., Wright, J. and Flatte, S.M. "Energy and Action Flow Through the Internal Wave Field: an Eikonal Approach," *Journal of Geophysical Research*, Vol. 91, No. C7, Pages 8487-8495, July 15, 1986
- 9) Henyey, F.S., Rouseff, D., Grochocinski, J.M., Reynolds, S.A., Williams, K.L. and Ewart, T.E., "Effects of Internal Waves and Turbulence on a Horizontal Aperture Sonar," *IEEE Journal of Oceanic Engineering*, Vol. 22, No. 2, April 1997
- 10) Duda, T.F., Bowlin, J.B., "Ray-Acoustic Caustic Formation and Timing Effects from Ocean Sound-Speed Relative Curvature," *J. Acoustic Soc. Am.*, Vol. 96, No. 2, Pt. 1, August 1994
- 11) Duda, T.F., Trivett, D.A., "Predicted Scattering of sound by diffuse hydrothermal vent plumes at mid-ocean ridges," *J. Acoustic Soc. Am.*, Vol. 103, No. 1, January 1998

THIS PAGE INTENTIONALLY LEFT BLANK

INITIAL DISTRIBUTION LIST

1. Dudley Knox Library
Naval Postgraduate School
Monterey, California
2. Prof. Kevin B. Smith (Code PH/Sk)
Department of Physics
Naval Postgraduate School
Monterey, California
3. Prof. Samuel E. Buttrey (Code OR/Sb)
Department of Operations Research
Naval Postgraduate School
Monterey, California
4. Prof. James N. Eagle (Code OR/Er)
Department of Operations Research
Naval Postgraduate School
Monterey, California
5. Dr. Ellen Livingston (Code 3210A)
Office of Naval Research
Arlington, Virginia
6. Dr. Peter H. Dahl
Applied Physics Laboratory
University of Washington
Seattle, Washington